

Title: AC magnetometry with active stabilization and harmonic suppression for magnetic nanoparticle spectroscopy and thermometry

Authors

Thin Q. Bui*, Weston L. Tew, Solomon I. Woods

National Institute of Standards and Technology (NIST), Gaithersburg, MD, USA 20899

*Author to whom correspondence should be addressed: thin.bui@nist.gov

Abstract

Magnetic nanoparticle (MNP) thermometry based on magnetic particle spectroscopy (MPS) is explored as a potential approach for realizing in-situ temperature measurement of 3D objects. MNP thermometry relies on the nonlinear magnetization response to an AC drive field. This nonlinear response has functional dependence on frequency and temperature, governed by the complex magnetization dynamics of MNPs suspended in solution. In this work, we introduce our approach for accurate and precise AC magnetization measurements using actively stabilized drive fields ranging from DC to 10 kHz. To isolate the harmonic response of MNPs from the drive field, we also perform active cancellation to reach drive field suppression up to 120 dB. Active stabilization and cancellation are utilized for real-time, sensitive measurements of AC magnetization of commercial samples, with stability on the timescale of hours. Initial results for MNP thermometry are demonstrated using this technique, and we achieved a total temperature uncertainty of 410 mK and 170 mK at 100 ms and 10 s integration time, respectively.

Introduction

Magnetic characterization of the dynamical properties of magnetic nanoparticles (MNPs) is an emerging field with applications ranging from material science to medicine¹⁻³. DC and AC magnetometry techniques are extensively utilized for understanding MNPs' intrinsic and extrinsic properties towards optimizing nanoparticle response for applications in biomedicine^{2, 4}, magnetic memory⁵, ferrofluids⁶, and those driven by fundamental interests. The dynamic response of MNPs in magnetic fields are intricate, and sometimes subtle, depending strongly on the particles' inherent properties, inter-particle interactions, as well as the environment in which they are suspended. Thus, comprehensive understanding of these effects requires high sensitivity over a broad parameter space. One important subset of AC magnetometry is magnetic particle spectroscopy (MPS), which was developed to determine the spectral response of MNPs used in magnetic particle imaging (MPI).⁷⁻¹¹ Experimental approaches for MPS have been reported in a number of publications and references therein.¹²⁻¹⁶

An underdeveloped application with immense potential using MNPs is non-invasive and remote temperature thermometry. Remote temperature measurement is well understood to be important in biology and medicine¹⁷⁻²¹, and could also be valuable for research in areas such as 3D printing, heat exchangers, and chemical synthesis. MNP thermometry relies on the temperature dependence of magnetization, $M(T)$. For obtaining the most sensitive thermometer, it is therefore desirable that the magnetization displays a strong temperature dependence such that the derivative

$(1/M)dM(T)/dT$ is as large as possible. There have been a number of reports of applications of MPS for MNP thermometry.^{19, 20, 22-25} In contrast to DC magnetometry-based MNP thermometry²³, AC drive fields interrogate the frequency-dependent dynamics that give rise to the observed magnetization signal. Especially important are the effects of relaxation dynamics (Néel and Brownian), which are not included in the quasi-static magnetization treatment as described by the Langevin function.²⁶⁻²⁹ These dynamics originate from a combination of intrinsic properties of the MNPs (e.g. anisotropy) and effects of their environment (e.g. viscosity, solvent, inter-particle interactions); both factors have functional dependence on temperature.

Successful application of AC magnetometry for MNP thermometry demands both high fidelity quantitative measurements and quantification of metrics for stability, especially in the context of the precision and accuracy of MNP magnetization measurements. To be a viable thermometer, a key metric is that the measured intrinsic magnetization of MNPs must be reproducible and independent of environmental conditions. In contrast to measurement of the full harmonic spectrum in MPS for magnetic particle imaging, thermometry typically requires the use of only two harmonics at a time.^{22, 24} A well-documented complication for quantitative MPS for AC magnetometry, thermometry, and imaging is the presence of the feedthrough (drive) signal at the detector, which can obfuscate the small MNP signal.^{15, 30} A number of studies report a gradiometer configuration for passive feedthrough subtraction on the order of ≈ 60 dB.³¹ Another common passive approach is electronic filtering of the feedthrough signal, which suppresses the 1st harmonic signal by ≈ 110 dB.³² A more recent and promising technique combined passive and active cancellation for broadband feedthrough suppression, though the methods do not permit real-time feedback and measurements.^{15, 33} Here, we report our method for real-time MPS with a drive field stability at the parts-per-million level and suppression of the feedthrough signal's 1st and 3rd harmonics by 120 dB, limited only by the detector noise floor. Finally, we demonstrate initial performance of our MPS for accurate measurement of temperature-dependent magnetization towards our goal of developing a magnetic nanoparticle-based thermometer.

Methods/Instrumentation

The MPS instrument consists of a Helmholtz coil pair for producing AC magnetic fields (Fig. 1A). The field amplitudes and frequency achievable are 10 mT_{RMS} (28 mT_{p-p}) for frequencies DC to 10 kHz driven by a function generator (Keysight 35000B³⁶) and amplified by a power amplifier (Accel TS250³⁶). Coil IC2 is used for measuring the drive field while IC1 is for measurement of the MNP sample. The ≈ 10 mm separation between IC1 and IC2 is sufficiently distant to avoid detectable MNP signal at IC2. Rather than directly using the two coils in a traditional gradiometric configuration, the two coils are kept independent for stabilization and feedthrough cancellation described in more detail in the following. A digital lock-in amplifier (SR865A³⁶) measures the amplitude and phase of the drive field 1st and 3rd harmonics from IC2. The amplitude of the 1st harmonic is used for stabilization of the drive field. In addition, the 1st and 3rd harmonic amplitude and phase are used for feedthrough subtraction of IC1. Real-time proportional-integral (PI) lock loops maintain the drive field stabilization and feedthrough subtraction.

In the drive field stabilization feedback lock, the 1st harmonic amplitude of IC2 is compared to a set-point, whose difference is the error signal used to control the amplitude of the function generator to keep the 1st harmonic amplitude stable at the set-point value. In contrast to this drive field stabilization feedback lock, the feedthrough signal cancellation is a feedforward-type lock which includes a second function generator to provide the feedforward cancellation signal. The 1st and 3rd harmonic amplitude and phase recorded by IC2, and after electronic filtering, are used to calculate an offset voltage and orthogonal phase to the IC1 signal. The correction signal sets the output value of a second function generator as the orthogonal amplitude and phase for both harmonics. The function generator's outputs for both harmonics are summed (SIM980)³⁶ and sent into one channel of the SR560³⁶ preamp. The IC1 signal is fed into the second channel of the preamp, and the differential output of the two channels is digitized with a PXI 5922³⁶ instrument (5x10⁴ samples per second, 24 bit). This configuration maintains active subtraction of the 1st and 3rd harmonics drive signal (IC2) from the MNP magnetization signal (IC1). Even though only the 1st and 3rd harmonic signals are actively subtracted, this procedure can in principle be extended for an arbitrary number of harmonics. In our experiment, we only use low magnetic field amplitudes (< 5 mTRMS) for thermal stability (to be discussed in following sections), which resulted in only background 1st and 3rd harmonics. Therefore, active suppression of the first two harmonics is sufficient to achieve a background-free MNP harmonic spectrum.

For measurement of temperature-dependent magnetization, a sample holder was machined from Shapal³⁶ ceramic and is shown in Fig. 1B. Two inductive coils (IC1, upper and IC2, bottom) are wound directly on the Shapal³⁶ mount where the MNP sample is situated. This sample mount is enclosed within a larger outer Shapal assembly where the temperature is controlled by liquid-coolant. Thermal contact between the two components are facilitated by silicone thermal grease. The outer assembly provides additional temperature isolation from ambient conditions. Four industrial 100 ohm platinum resistance thermometers (PRTs, Sensing Devices Inc., PT100³⁶) with thermometric tolerance $\Delta T < 0.13 \text{ K} + 0.0005|T - 273.15 \text{ K}|$ are situated on the body of the outer assembly to provide information on temperature stability and thermal gradients in the system. For all measurements described in this work, the MNPs used are Ocean Nanotech SHP15 (5 mg Fe/ml in 300 μl)³⁶, Vivotrax (5 mg Fe/ml in 300 μl)³⁶, and 50 nm Micromod Synomag (10 mg Fe/ml in 300 μl)³⁶.

Results and Discussion

I. Drive field stabilization

To achieve reproducible measurements of MNP magnetization, it is important that the magnetic excitation field be stabilized and fixed to a known value. The measurement scheme is shown in Fig. 1A. The feedback loop filter is implemented digitally in LabVIEW³⁶ to maintain constant 1st harmonic at IC1 by adjusting the current to the drive coils. Fig. 2A shows the stabilized drive intensity (2.5 mTRMS, 772 Hz) for a lock bandwidth of ≈ 100 Hz. Higher bandwidths did not impact the signal stability, since the drifts are mainly driven by slow time scale thermal processes. Feedback bandwidths at 30 Hz or less resulted in a noisier drive signal by a factor of 2, a timescale consistent with a thermal drift process. At 2.5 mTRMS drive amplitude, the magnetic field is stable for greater than 1 h with a stability of 40 nTRMS, or 16 $\mu\text{TRMS/TRMS}$. With the lock disengaged

(≈ 4400 s), the intensity drifts almost immediately from thermal effects, as shown in Fig 2A. The 1σ Allan deviation (Fig. 2B) plot reveals that the system is dominated by random statistical noise for integration times > 10 s before thermal effects cause random walk drifts. Random (statistical) noise follows a $\tau^{-1/2}$ dependence, where τ is the averaging time, as indicated by the dashed curve in the plot. Compared to the unlocked case, the Allan deviation for the locked field intensity shows an improvement by a factor of greater than 3 for 10 s integration time. Finally, drive fields at other frequencies (2427 Hz, 5917 Hz) display similar behavior at sufficiently low drive amplitudes (≈ 2.5 mTRMS). At higher amplitudes and higher frequencies, the AC resistance of the drive coils causes uncontrollable heating and eventually thermal runaway (to be discussed in later sections).

II. Harmonic cancellation

The feedthrough cancellation of the largest harmonics, the 1st and 3rd harmonics, is implemented by a feedforward lock. Here, we achieve a typical feedthrough attenuation greater than 100 dB, with a maximum measured attenuation of 120 dB (Fig. 3A-3C), performing in real-time. For example, the amplitude of the drive field at 772 Hz (Fig. 3A) is 0.85 V compared to the suppressed amplitude of ≈ 2 μ V. The use of IC2 to cancel the feedthrough of IC1 requires that the signals are highly correlated, which was verified by measuring the response of two IC signals over time. Temporal drifts in both the amplitude and phase of the feedthrough signal in the IC2 will result in a feedthrough signal above the detector noise floor, thus control of both variables is required for optimal, continuous feedthrough suppression. Due to the correlation of amplitude and phase in the feedthrough cancellation loop, the magnetic field intensity lock helps to stabilize the feedforward lock by eliminating the amplitude drift.

The best performance was observed with a bandwidth of the feedforward lock of 100 Hz for the 1st harmonic (limited by the intensity lock bandwidth) and 30 Hz for the third harmonic (limited by the SNR of the 3rd harmonic lock-in detection). Figure 4A show the time-dependent feedthrough signal of the 1st harmonic amplitude recorded at 100 ms integration time for the scenarios with (active) and without (passive) the feedforward loop engaged (no sample in IC1). In the passive case, the feedthrough signal is subtracted manually by adjusting the amplitude and phase from the function generator, then left alone over time. In the active case, the feedforward loop is engaged continuously. Drifts in both the amplitude and phase cause the signal to deviate from the minimal feedthrough signal (time zero on black trace) nearly immediately after the lock is disengaged. The Allan deviation of the 1st harmonic feedthrough signal for the blank and MNP sample display similar temporal stability limited by the intensity stabilization lock loop (Fig. 4B).

External, environmental factors may perturb the correlation between IC1 and IC2 and cause drifts in the feedthrough suppression signal. These factors include external magnetic fields, mechanical vibrations, and temperature drifts. Noise from external magnetic fields can readily be suppressed by shielding in a Faraday cage. Temperature drifts are only passively controlled by the flow of air currents. To test the impact of mechanical disturbance, an MNP sample was introduced and removed while the system was locked. Fig. 4C shows the resulting 1st harmonic signal, demonstrating that the original cancellation can be achieved after cycles of introducing and removing of the MNP sample in a glass vial, and a feedthrough cancellation of > 110 dB is maintained for subsequent MNP measurement. The baseline, feedthrough-subtracted, value is \approx

$29.7 \mu\text{V}_{\text{RMS}} \pm 14 \mu\text{V}_{\text{RMS}}$. With the MNP sample introduced, the feedthrough-subtract signal is $\approx 1.03 \text{ mV}_{\text{RMS}} \pm 17.8 \mu\text{V}_{\text{RMS}}$. The uncertainty in the feedthrough attenuation level is limited by the sum of uncorrelated noise sources from the inductive coil, voltage summer, and the preamplifier.³⁴ Using these noise sources, the noise density is calculated to be $70 \text{ nV}_{\text{RMS}}/\text{Hz}^{1/2}$ and measured to be $\approx 100 \text{ nV}_{\text{RMS}}/\text{Hz}^{1/2}$ (black trace, Fig. 3B). In this calculation, the voltage summer voltage noise ($60 \text{ nV}_{\text{RMS}}/\text{Hz}^{1/2}$) has the largest noise contribution, followed by the voltage noise of the preamplifier ($4 \text{ nV}_{\text{RMS}}/\text{Hz}^{1/2}$). The calculated noise value differs from the measured value because it does not account for the noise pedestal (phase noise of the oscillator) near the drive (carrier) frequency of the amplified function generator signal. This noise pedestal is evident in the comparison of the “blank” measurement, or feedthrough-subtracted signal (black), to the “noise level”, when the drive field is removed (blue). For a 50 kHz acquisition rate, the integrated noise (baseline in Fig. 4C) for a noise density $70 \text{ nV}_{\text{RMS}}/\text{Hz}^{1/2}$ corresponds to $15.6 \mu\text{V}_{\text{RMS}}$, which agrees with the measured noise values for the baseline and MNP signal.

III. Stability of real-time magnetization measurement

By performing real-time cancellation of the 1st and 3rd harmonic feedthrough signal, the measurement of the 1st and 3rd harmonic MPS signals are obtained nearly background-free (without drive signal interference). For the highest SNR measurement, we are mainly interested in the low energy harmonics, which dominate at relative low driving field $< 10 \text{ mT}_{\text{p-p}}$. An additional advantage to using low amplitude drive field is that the system is less prone to thermal drifts caused by heating of the drive coils, a significant source of system instability. Coil heating is exacerbated at high driving frequencies due to the increasing reactance of the coils and is difficult to control. The intensity stabilized drive field at 772 Hz for a 2000 s segment is shown in Fig. 4A. For 4000 s (from Fig. 2A), the stability of drive field is $2.5 \text{ mT}_{\text{RMS}} \pm 14 \text{ nT}_{\text{RMS}}$ ($\approx 7 \text{ mT}_{\text{p-p}} \pm 39 \text{ nT}_{\text{p-p}}$). We confirm this stability by measuring the Allan deviation of both the subtracted feedthrough signal and the MNP signal shown in Fig. 4B. The Allan deviation curves with and without the sample display expected similar noise behavior with integration time, with the optimal integration times limited by the stability of the drive field lock loop (Fig. 2B). However, because the subtracted feedthrough signal is IC1 – IC2, any disturbance in the correlation of the two ICs would manifest as differential noise and result in systematic drifts at the characteristic timescale of the noise source. In our case, differential noise results in the observed drift at the 2 s timescale in Fig. 4B. We anticipate that if the two ICs were perfectly insulated from the environment and temperature stabilized (e.g. in a vacuum chamber), the temporal stability of the signals would significantly improve.

IV. Noise of magnetization measurement

Complementary to time-dependent noise analysis, noise spectral density characterization via Fourier transform is useful for revealing frequency-dependent noise sources. Noise at three resonant drive frequencies was measured (772 Hz, 2.427 kHz, and 5.917 kHz) at $\approx 2.5 \text{ mT}_{\text{RMS}}$ ($\approx 7.1 \text{ mT}_{\text{p-p}}$) drive amplitude. In an idealized gradiometer, all common-mode noise sources would cancel out, leaving behind only residual statistical noise. Our method of direct cancellation of 1st and 3rd harmonic feedthrough signal does not suppress all noise sources outside of the single-tone harmonics. This can be observed from a spectral noise density plot. In Figures 3, the amplitude spectral density (ASD) for the blank (feedthrough suppression with drive signal), background (no

drive signal), and MNP (feedthrough suppression + MNP signal) signals are displayed. The ASD signals were computed from the Fourier transform of the time-dependent magnetization signal and accounting for an equivalent noise bandwidth with a Hanning window, an acquisition rate of 5×10^4 samples per second, and sample length of 5×10^4 samples. Figures 3A, 3B, and 3C indicate that the real-time feedthrough suppression of the targeted 1st and 3rd harmonics reaches the noise floor of the detector, values ranging from $100 \text{ nV}_{\text{RMS}}/\text{Hz}^{1/2}$ to $1000 \text{ nV}_{\text{RMS}}/\text{Hz}^{1/2}$ at 772 Hz to 5917 Hz. Other frequencies are unaffected. Therefore, this method has the advantage of high suppression of the large feedthrough signals in real time at the expense of residual noise at non-targeted frequencies. The best way to capitalize on all the benefits of this approach is by implementing lock-in detection at only the largest harmonics (e.g. 1st, 3rd, and 5th) harmonic of the MNP signal to approach noise-immunity.

V. Time/Frequency MPS

In MPS, MNPs are typically driven by a sinusoidal waveform, even though recent implementations have explored various other waveforms.³¹ With sufficient drive amplitude, the MNPs are driven toward saturation, resulting in a spectrum populated by N higher harmonics of significant strength, with N depending on the value of the field amplitude relative to the field required to magnetically saturate the MNPs. Both the time and frequency domain representation convey the same information and can be used to understand the MNP magnetization under AC drive fields in MPS. Using inductive coils, the observed signal is the time derivative of the magnetization signal. Fig. 5A show the IC signals ($dM(t)/dt$) at increasing drive amplitude for 50 nm Micromod Synomag³⁶ particles at a drive frequency of 2427 Hz, and the corresponding magnetization (Fig. 5B). Due to the active cancellation of the 1st and 3rd harmonics of the drive field, the time-dependent, magnetization response of MNPs at small drive amplitudes, which are dominated by low harmonics, are observable rather than being obscured by the drive field.

To measure the hysteresis loop, the phase lag of the MNP signal with respect to the drive field must be known. The phase lag at each different frequency (772 Hz, 2427, and 5917 Hz) was determined by measuring the phase of the blank gradiometric signal (IC1 – IC2) with the feedforward lock turned off so that there would be a residual IC1 – IC2 signal. When the MNP sample is present, the phase shift relative to the residual gradiometric signal determines the phase lag of the sample response with respect to the drive field. This approach for correcting phase shifts properly accounts for time delays introduced by the cable length and electronic components between the signal and the digitizer. With the phase shift correction applied, the hysteresis loops are obtained by plotting the $M(t)$ as a function of drive field, $\mu_0 H(t)$. The results for Ocean Nanotech SHP15³⁶, Vivotrax³⁶, and 50 nm Micromod Synomag³⁶ magnetic nanoparticles are plotted in Fig. 5C.

VI. Magnetic Nanoparticle Thermometry

For measurement of the temperature-dependent magnetization, 300 μL of 5 mg Fe/ml Vivotrax³⁶ sample is sealed in a sapphire crucible to avoid changing the particle concentration upon evaporation, especially during heating. The sapphire crucible is chosen for its high thermal conductivity to ensure uniform temperature equilibration of the MNP liquid sample volume. The

crucible is seated within the Shapal³⁶ mount, and the two objects are thermally contacted by silicon-based thermal grease. The crucible is further isolated from the ambient environment (e.g. air currents) by an O-ring-sealed lid. Four 100 ohm PRTs are used to measure the temperature of the Shapal³⁶ sample holder (Figure 1). Due to the physical separation between the measurement PRTs and the MNP sample, it is necessary to 1) verify that the MNP sample reaches thermal equilibrium with the Shapal³⁶ mount and 2) quantify the magnitude of a temperature gradient between the PRT and MNP sample sites. For this offset measurement, a distilled water-filled sapphire crucible with an immersed 100 ohm PRT was positioned at the center location of the mount. The distilled water-filled crucible acted as a proxy to the actual MNP sample that is also suspended in an aqueous solution. This measurement showed that the MNP sample's temperature agrees to within 100 mK of the PRTs located near the edge over the tuning range of 275 K to 310 K.

Temperature-dependent magnetization was measured using the 3rd and 5th harmonics of the 2427 Hz (2.5 mTRMS) drive field. The drive field was actively stabilized at 2.5 mTRMS using the IC2 signal. IC1 measures the MNP harmonic response. The 1st harmonic response displayed strong dependence on temperature, likely due to the temperature dependence of the inductive coil causing differential noise in IC1 and IC2. This prevented reliable measurement of temperature-dependent magnetization using the 1st harmonic via the active cancellation technique. As an alternative to the active cancellation technique, we used the difference signal (IC1-IC2) in a typical gradiometer configuration. While this does not suppress the 1st harmonic drive field, the 3rd and the 5th harmonics of MNPs are well isolated from the drive field (Fig. 5A). The 3rd harmonic signal is greater by a factor of $\approx 10^2$ with sample compared to the background drive field. The 5th harmonic signal from the drive field is below the IC noise floor, so the detectable 5th harmonic signal originates only from MNPs.

Magnetization response was measured after the four PRTs reached ± 25 mK stability (≈ 15 min at each temperature) to ensure that the sample is in thermal equilibrium with the mount. At each temperature, the 3rd and 5th harmonics of both IC1 and IC2 are recorded. Since IC2 measures the drive field only, the signal from IC1 was corrected for drifts in IC2 to isolate only the temperature dependent magnetization response from the MNP sample. To verify that the signal originates only from MNPs and not from other experimental systematics (e.g. temperature-dependences of the inductive coils), we perform the same measurement without the MNP sample at each temperature. These blank measurements of the 3rd and 5th harmonic amplitudes resulted in a flat, temperature-independent response. Finally, the equilibrated temperatures were randomly sampled (not monotonically sampled) to avoid possible systematics associated with a linear temperature ramp.

The temperature precision of Vivotrax³⁶ as a thermometer was quantified at 2427 Hz (2.5 mTRMS) drive field. Figures 6B and 6C show the magnetization versus temperature for the 3rd and 5th harmonics. Note that the blank measurements have an arbitrarily added offset for clarity. Each data point is the average of an ensemble of 10^4 lock-in measurements at a rate of 100 Hz (100 seconds integration time), and 100 measurements of the PRT temperature (average value from the 2 upper PRTs) at a rate of 1 Hz. The temperature uncertainty is determined by the

measurement precision of the induced magnetization of MNPs detected by the inductive coil 1 (IC1) and the temperature of the MNP sample measured by the PRT. The corresponding Allan deviation plots for the 3rd and 5th harmonic amplitude of MNP samples as a function of integration time provide the key metric for precision. The temperature uncertainty from MNP magnetization measurement is obtained by dividing the Allan deviation (δV) at a specified integration time by the slope of magnetization versus temperature ($\delta V/\delta T$) curve (in Fig. 6D). The corresponding statistical component of the temperature uncertainty, δT_v , from δV at 100 ms integration time is 373 mK using the 3rd harmonic and 1.7 K using the 5th harmonic. The contrasting magnitude of δT_v for the harmonics is mainly dictated by the differing slopes of the temperature-dependent magnetization curves. To further demonstrate the advantage of long-term stability for our system, the Allan deviation at the optimal 10 s integration time leads to a significant reduction in the temperature uncertainty to 46 mK and 196 mK for the 3rd and 5th harmonics, respectively. Along with the temperature uncertainty from the inductive coil voltage (δT_v) measurement, additional sources of uncertainty from the PRT temperature measurement (δT_{PRT}) and our noise analysis contribute to the total uncertainty of MNP thermometry. The dominant sources of statistical and systematic errors for the measurement of V and T used to determine the total temperature uncertainty for an integration time of 100 ms are summarized in Table 1.

The magnetization response of magnetic nanoparticles under AC driving fields are known to display complex behavior depending on the drive amplitude, frequency, and temperature.³⁵ At AC frequencies, the magnetization signal is dependent on the relaxation dynamics governed by both Néel and Brownian motion. Depending on the dominant relaxation process, the magnetization amplitude can either decrease or increase with temperature.²⁶ In our case, we observe decreasing magnetization at increasing temperature up to frequencies of ≈ 10 kHz, indicating that our Vivotrax samples are thermally randomized from DC to 10 kHz. We seek to perform a more thorough study of the frequency- and temperature-dependent dynamics using an arbitrary-waveform relaxometer system currently in development.³¹

Conclusion

In this work, we introduce a magnetic nanoparticle spectrometer for accurate characterization of MNP magnetization response. With the targeted application of MNP thermometry, our method for active stabilization and cancellation of low energy harmonics of the drive field provides a direct approach for obtaining the most information-rich signals from the total harmonic response. Moreover, our technique allows for real-time measurements of AC magnetization with long-term stability, enabling highly reproducible characterization of MNP response. Accurate temperature measurements based on our technique may be applied towards magnetic hyperthermia in which MNPs are heated by an additional high amplitude, high frequency AC field (> 100 kHz). The large separation of the two frequencies may facilitate simultaneous heating and monitoring in magnetic hyperthermia since the fields drive the MNP dynamics in an independent fashion (at significantly different characteristic timescales). In upcoming work, we will seek to expand this technique for covering broadband frequencies by performing agile frequency sweeps for thorough characterization of MNP dynamics for applications of thermometry and thermal imaging.

This is the author's peer reviewed, accepted manuscript. However, the online version of record will be different from this version once it has been copyedited and typeset.
PLEASE CITE THIS ARTICLE AS DOI: 10.1063/5.0031451

Acknowledgements

The authors acknowledge funding from NIST's Innovations in Measurement Science grant. We thank Cindi Dennis, Adam Biacchi, and Angie Hight Walker for helpful discussions. We thank Aaron Young for machining work, and Kevin Douglass for loaned equipment.

Data Availability

The data that support the findings of this study are available from the corresponding author upon reasonable request.

This is the author's peer reviewed, accepted manuscript. However, the online version of record will be different from this version once it has been copyedited and typeset.
PLEASE CITE THIS ARTICLE AS DOI: 10.1063/5.0031451

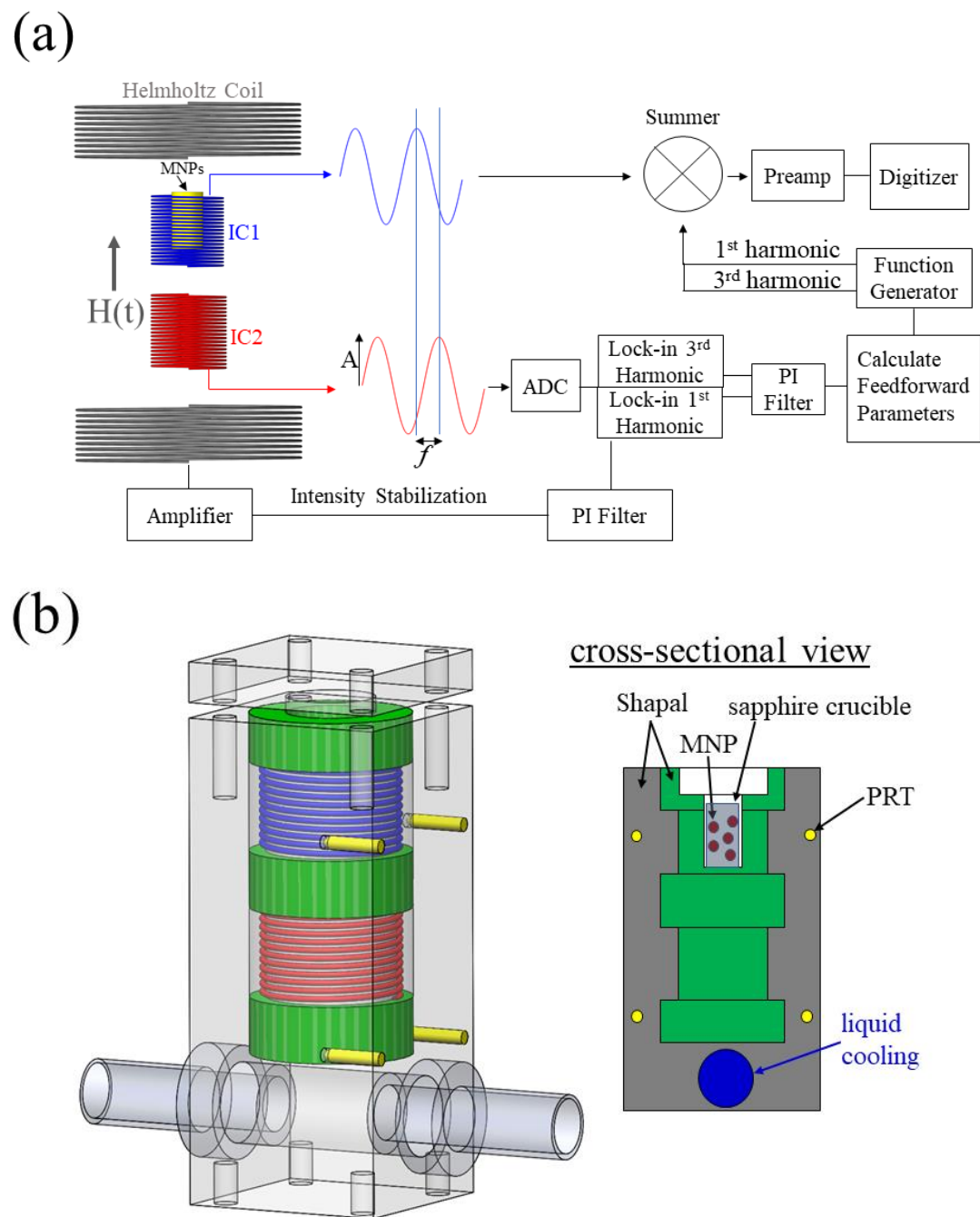


Figure 1: (a) MPS spectrometer with active drive-field stabilization and 1st and 3rd harmonic subtraction. The drive field is generated by Schwarzbeck³⁶ Helmholtz coil (gray). IC1 is used to measure MNP magnetization, and IC2 is used for active stabilization and drive field cancellation. (b) Mount for MNP thermometry. The outer Shapal mount (25.4 x 25.4 x 60 mm) is temperature tuned by a recirculating chiller via tubing at the base. In green is a Shapal sample holder (length = 42 mm, OD = 20 mm) with two inductive coils, IC1 (top, blue) and IC2 (bottom, red). IC1 and IC2 (OD = 15 mm, length = 15 mm) are separated by 10 mm. The sapphire crucible holding the MNP sample is positioned inside IC1. Four PRTs (yellow) measure the temperature and monitor thermal gradients of the Shapal mount.

This is the author's peer reviewed, accepted manuscript. However, the online version of record will be different from this version once it has been copyedited and typeset.
PLEASE CITE THIS ARTICLE AS DOI: 10.1063/5.0031451

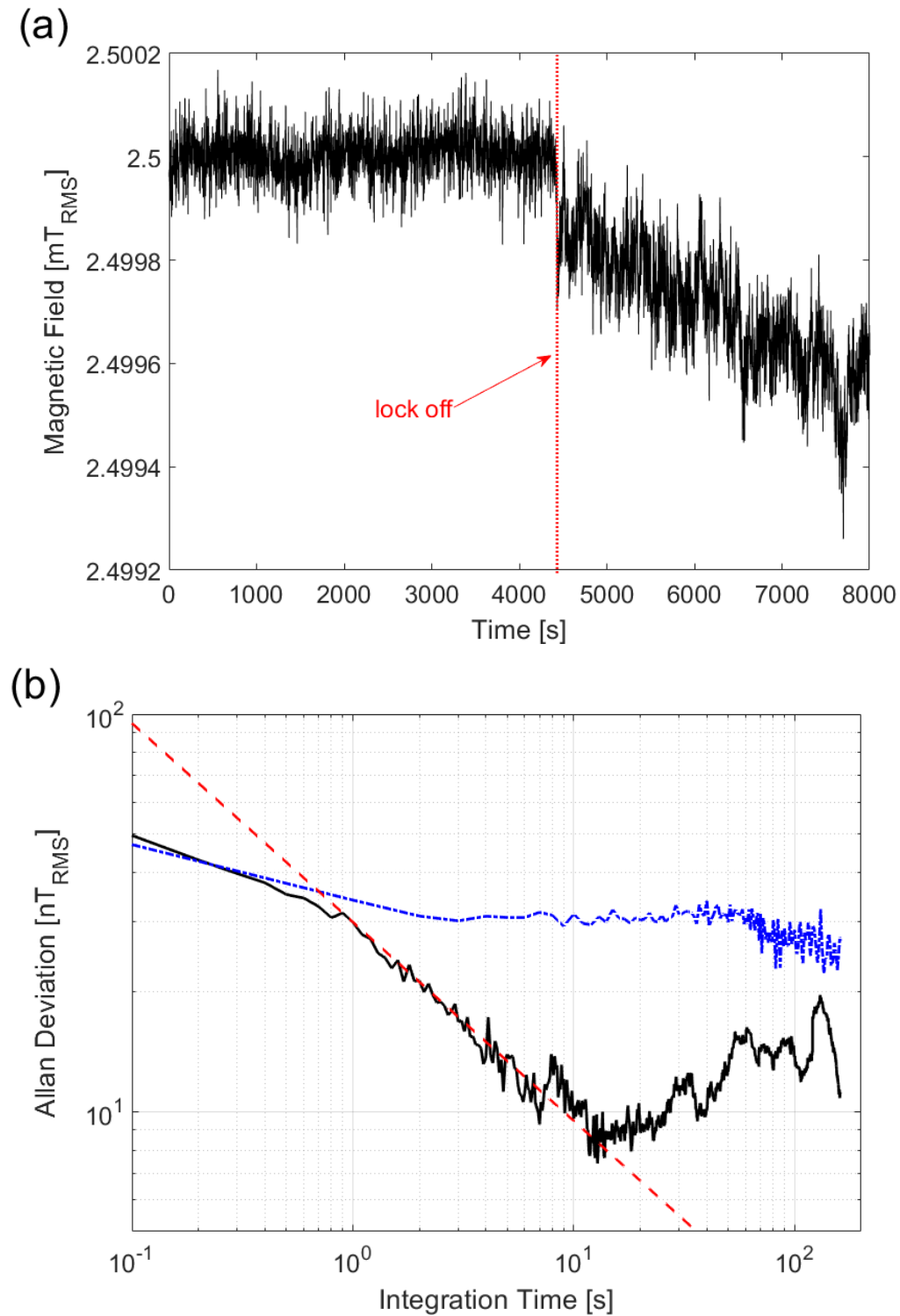
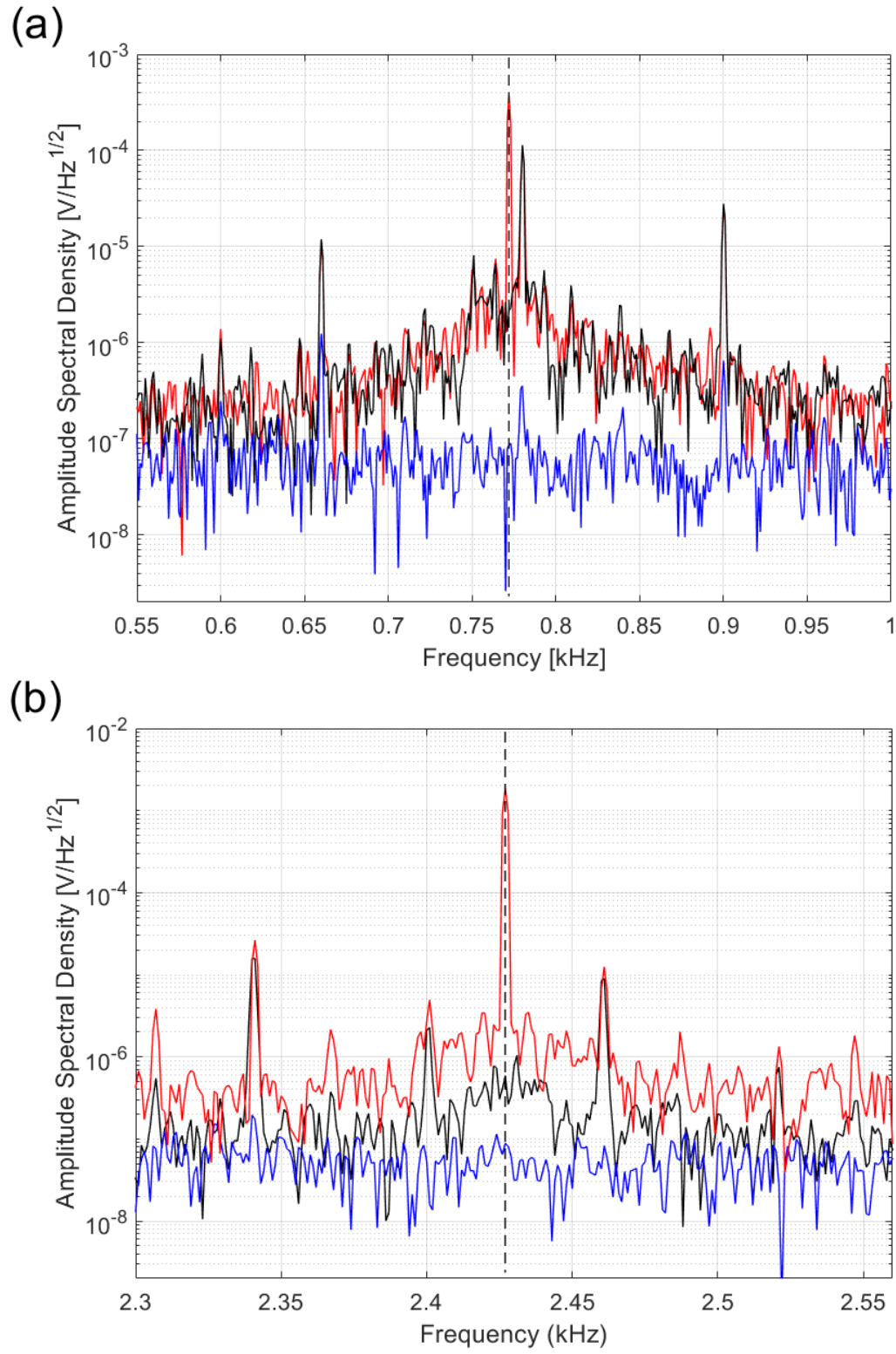


Figure 2: (a) Drive field stabilization lock at 772 Hz (2.5 mT_{RMS}). The conversion factor to convert the inductive coil signal to magnetic field amplitude was obtained from a calibrated teslameter (Lakeshore, F41³⁶). (b) Allan deviation of drive field at 772 Hz (2.5 mT_{RMS}). The black trace shows the drive field stabilization lock engaged, and the blue trace is for the unlocked (free-running) case. The red dashed-line is the $\tau^{-1/2}$ dependence, where τ is the integration time.

This is the author's peer reviewed, accepted manuscript. However, the online version of record will be different from this version once it has been copyedited and typeset.
PLEASE CITE THIS ARTICLE AS DOI: 10.1063/5.0031451



This is the author's peer reviewed, accepted manuscript. However, the online version of record will be different from this version once it has been copyedited and typeset.
PLEASE CITE THIS ARTICLE AS DOI: 10.1063/5.0031451

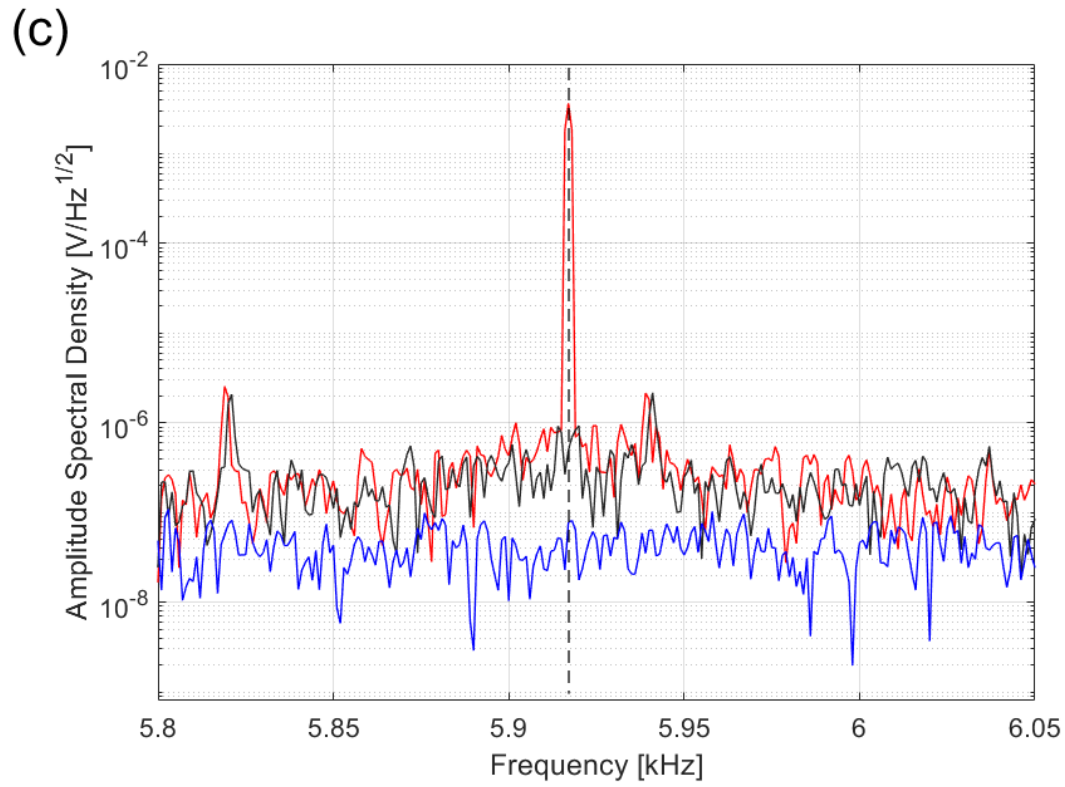
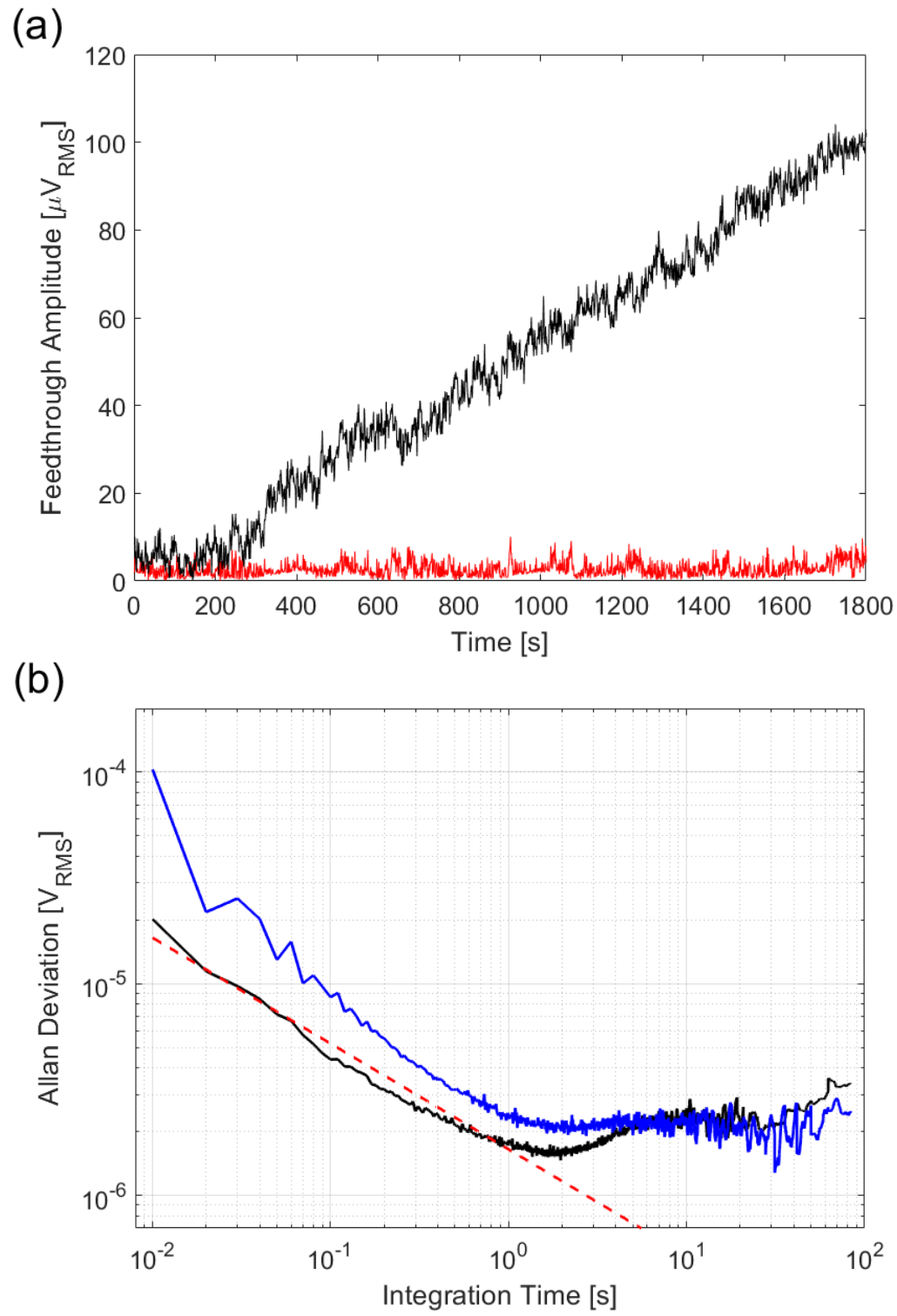


Figure 3: (a) Amplitude spectral density (ASD) at 772 Hz drive field (dashed vertical line), with real-time subtraction of the drive field 1st and 3rd harmonics. Data are shown for the cases of feedthrough suppressed drive signal with sample (red, 50 nm Synomag) and no sample (black), as well as the background case with no drive signal (blue). Note that the 780 Hz peak apparent in the black trace is due to noise from AC power line (13th harmonic of 60 Hz line noise). (b) Amplitude spectral density (ASD) at 2427 Hz drive field (dashed vertical line) (c) Amplitude spectral density (ASD) at 5917 Hz drive field (dashed vertical line).

This is the author's peer reviewed, accepted manuscript. However, the online version of record will be different from this version once it has been copyedited and typeset.
PLEASE CITE THIS ARTICLE AS DOI: 10.1063/5.0031451



This is the author's peer reviewed, accepted manuscript. However, the online version of record will be different from this version once it has been copyedited and typeset.
PLEASE CITE THIS ARTICLE AS DOI: 10.1063/5.0031451

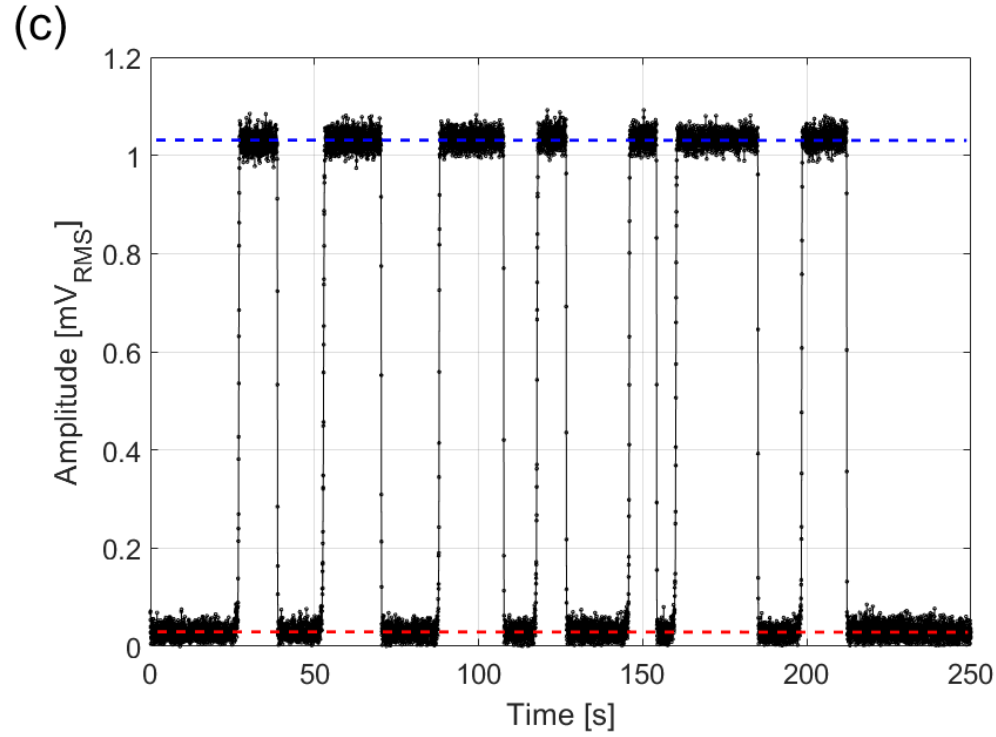
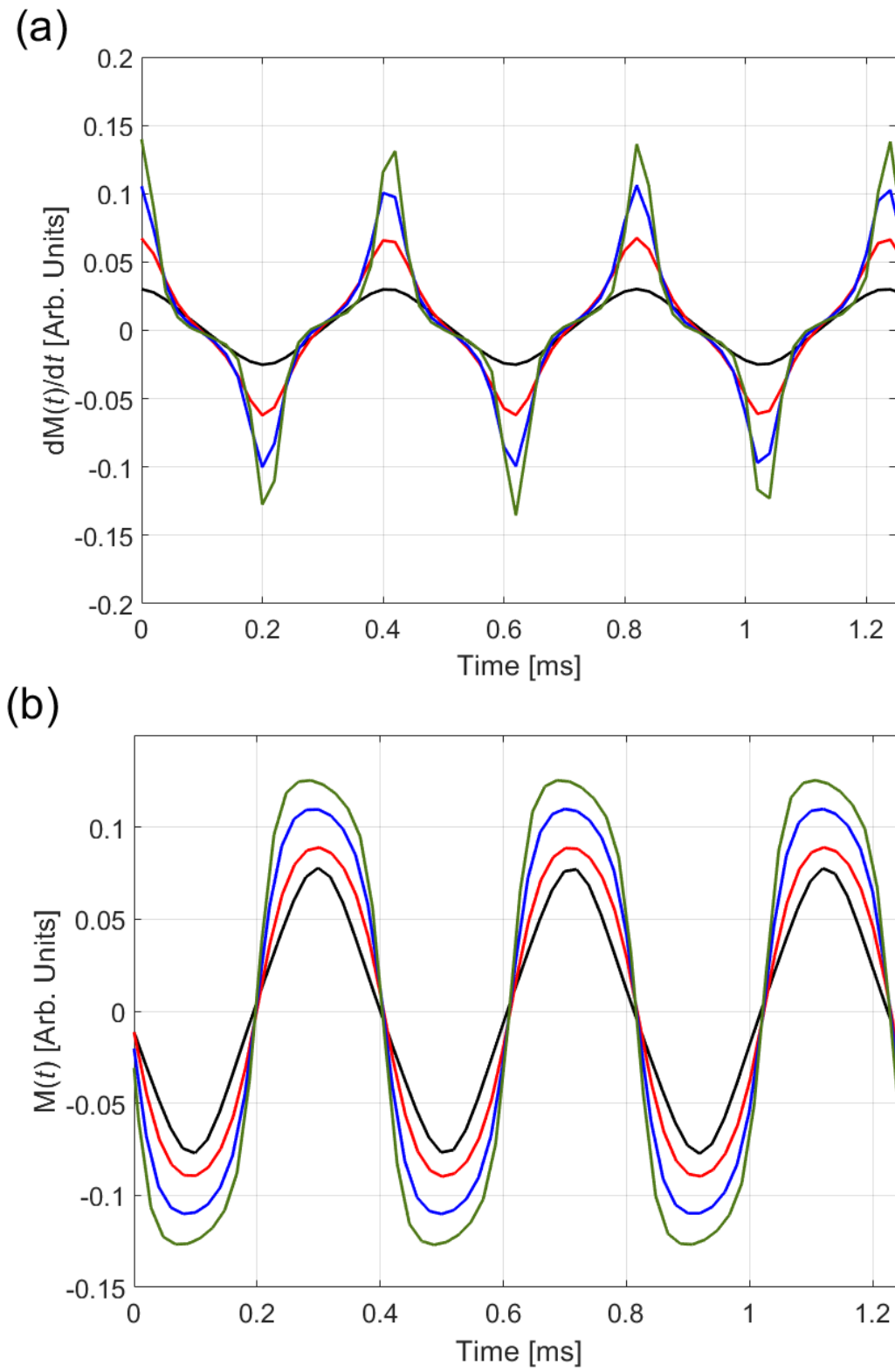


Figure 4: (a) Feedthrough signal with (red) and without (black) feedforward cancellation at 772 Hz ($2.5 \text{ mT}_{\text{RMS}}$) for a “blank” case without MNP sample. (b) Allan deviation of feedthrough signal with and without MNPs at 772 Hz ($2.5 \text{ mT}_{\text{RMS}}$). The blue trace is MNP sample (Vivotrax), and the black trace is the blank measurement. The red dashed line is the $\tau^{(-1/2)}$ dependence. (c) Real-time measurement of MNPs with intensity stabilization and feedforward cancellation, as the sample vial is inserted and removed from the instrument (blue level = Vivotrax sample, red level = blank). 1st harmonic signal measurements were performed at 772 Hz ($2.5 \text{ mT}_{\text{RMS}}$).

This is the author's peer reviewed, accepted manuscript. However, the online version of record will be different from this version once it has been copyedited and typeset.
PLEASE CITE THIS ARTICLE AS DOI: 10.1063/5.0031451



This is the author's peer reviewed, accepted manuscript. However, the online version of record will be different from this version once it has been copyedited and typeset.
PLEASE CITE THIS ARTICLE AS DOI: 10.1063/5.0031451

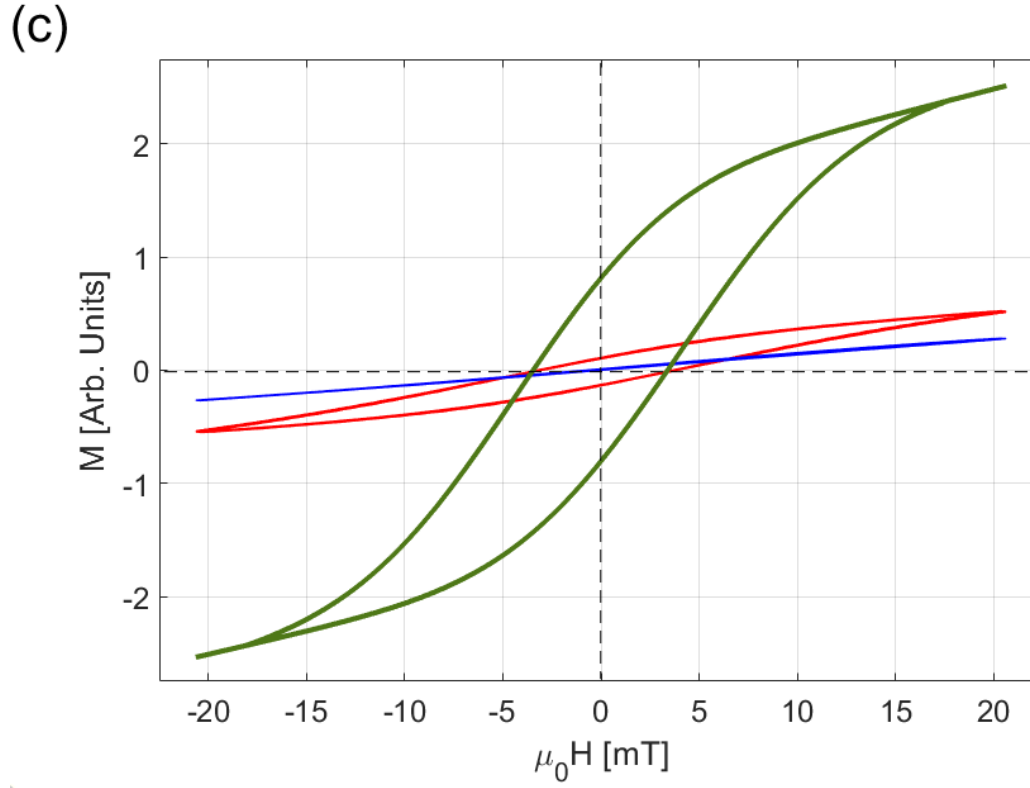
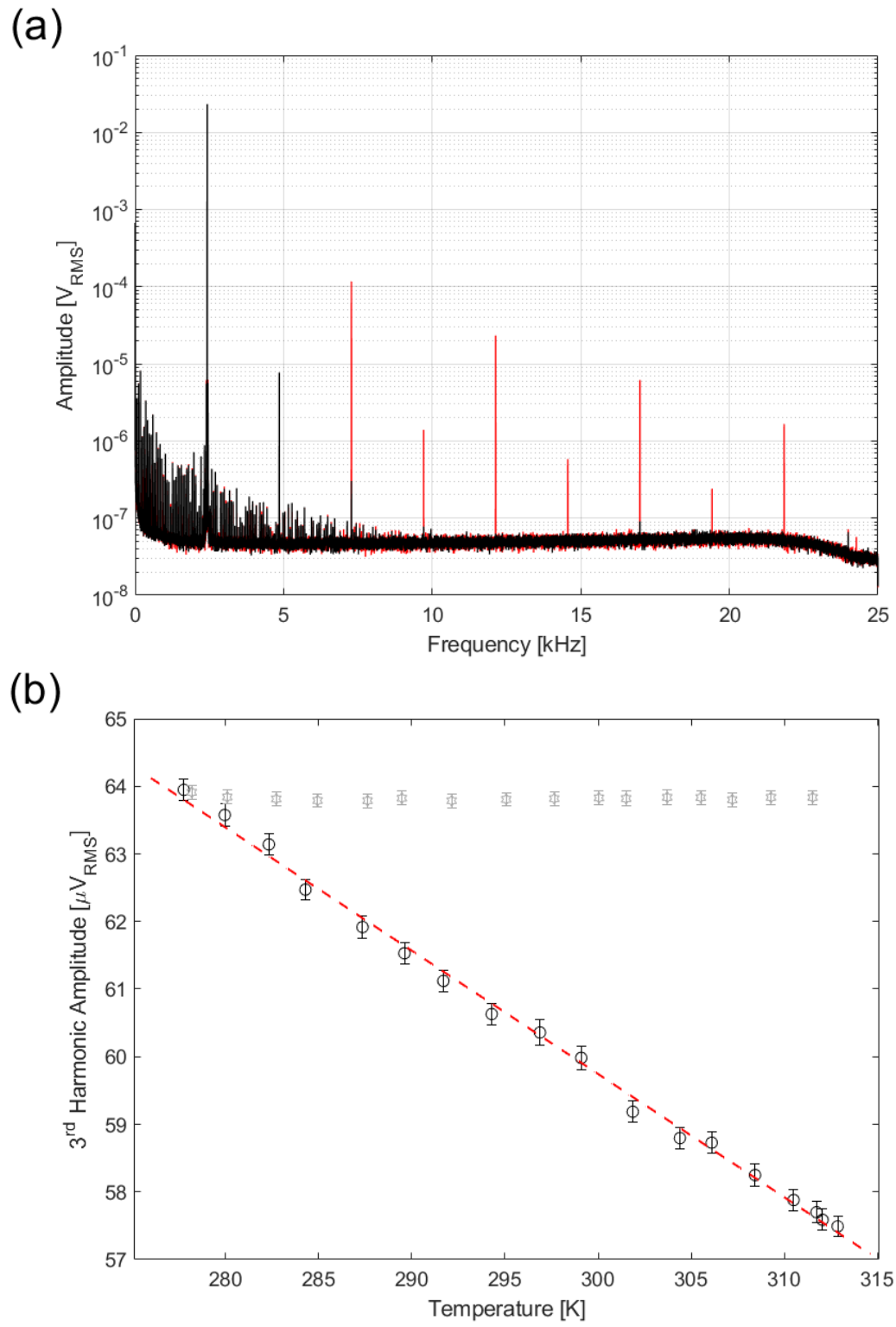
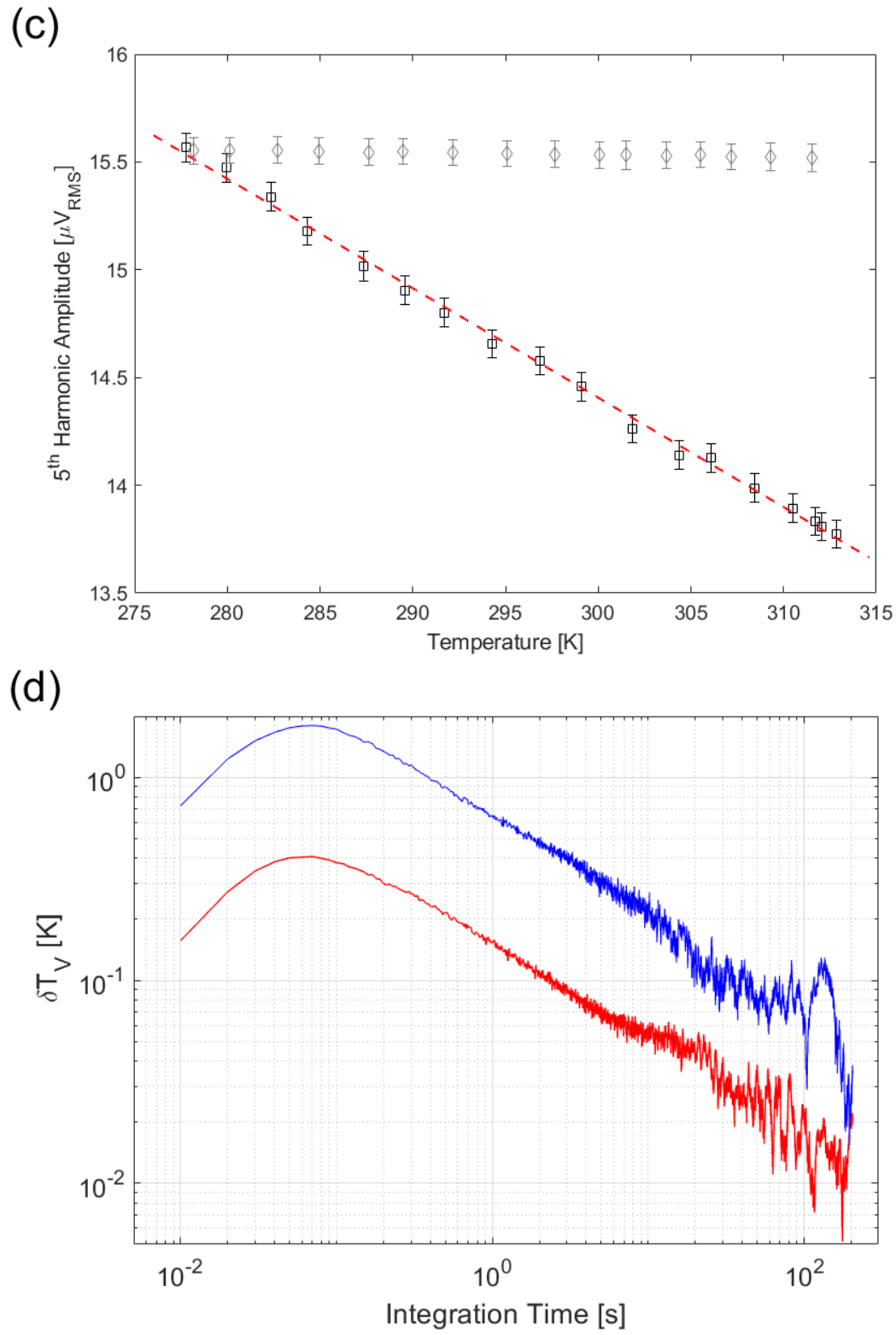


Figure 5: (a) Inductive coil signal ($dM(t)/dt$) for 50 nm Synomag at 2427 Hz. Black: 1.25 mT_{RMS}. Red: 2.5 mT_{RMS}. Blue: 5 mT_{RMS}. Green: 7.5 mT_{RMS}. (b) $M(t)$ for 50 nm Synomag at 2427 Hz. Black: 1.25 mT_{RMS}. Red: 2.5 mT_{RMS}. Blue: 5 mT_{RMS}. Green: 7.5 mT_{RMS}. (c) Hysteresis curve for 15 nm SHP15 (blue), Vivotrax (red), and 50 nm Synomag (green).

This is the author's peer reviewed, accepted manuscript. However, the online version of record will be different from this version once it has been copyedited and typeset.
PLEASE CITE THIS ARTICLE AS DOI: 10.1063/5.0031451



This is the author's peer reviewed, accepted manuscript. However, the online version of record will be different from this version once it has been copyedited and typeset.
PLEASE CITE THIS ARTICLE AS DOI: 10.1063/5.0031451



This is the author's peer reviewed, accepted manuscript. However, the online version of record will be different from this version once it has been copyedited and typeset.
PLEASE CITE THIS ARTICLE AS DOI: 10.1063/1.50031451

Figure 6: (a) Blank (black) and Vivotrax (red) spectrum at 2427 Hz (2.5 mT_{RMS}) for magnetization vs temperature measurement. The 3rd harmonic is 7.281 kHz and the 5th harmonic is 12.135 kHz. (b) Vivotrax 3rd harmonic amplitude (black circle) vs temperature at 2427 Hz, 2.5 mT_{RMS}. The slope ($\delta V/\delta T$) is -0.18(3) $\mu\text{V}/\text{K}$. The red dashed line is a linear regression to the data. The gray trace shows the blank measurement. An arbitrary 50 μV offset was added to the blank (gray) measurement to put the two traces on the same scale for clarity. The error bars are the 1σ standard deviation for an ensemble of 10^4 measurements for 100 seconds. (c) Vivotrax 5th harmonic amplitude (black square) vs temperature at 2427 Hz, 2.5 mT_{RMS}. The slope ($\delta V/\delta T$) is -0.051(1) $\mu\text{V}/\text{K}$. The red dashed line is a linear regression to the data. An arbitrary 10 μV offset was added to the blank (gray) measurement to put the two traces on the same scale for clarity. (d) Allan deviation (δT_V) of Vivotrax temperature for the 3rd harmonic (red) and 5th harmonic (blue) signals at 2427 Hz drive field. δT_V for each harmonic is obtained by dividing the measured δV by the slope ($\delta V/\delta T$) from figures 6B and 6C. Note that δT_V corresponds to temperature uncertainty due only to the measurement of the voltage induced by the MNPs on the inductive coil sensor.

δT Source	3rd harmonic	5th harmonic
δT_V	0.37	1.70
δT_{PRT}	0.13	0.13
Linear Regression	0.05	0.02
PRT Tolerance	0.13 K+0.0005 $\times T-273.15$ K	
Total δT_{total} (K) at 100 ms	0.41	1.70

Table 1: Error sources (units in Kelvin) for determining the total temperature uncertainty (δT_{total}) at 100 ms integration time. δT_V is uncertainty from the MNP signal (voltage) measured by the inductive coil (Fig. 6D). δT_{PRT} is the uncertainty from temperature measurements with the PRTs. The linear regression error is from the linear fit to the data in Fig. 6B and 6C. The PRT tolerance is the manufacturer-reported conformity of the PRT sensors to a nominal calibration curve.

References

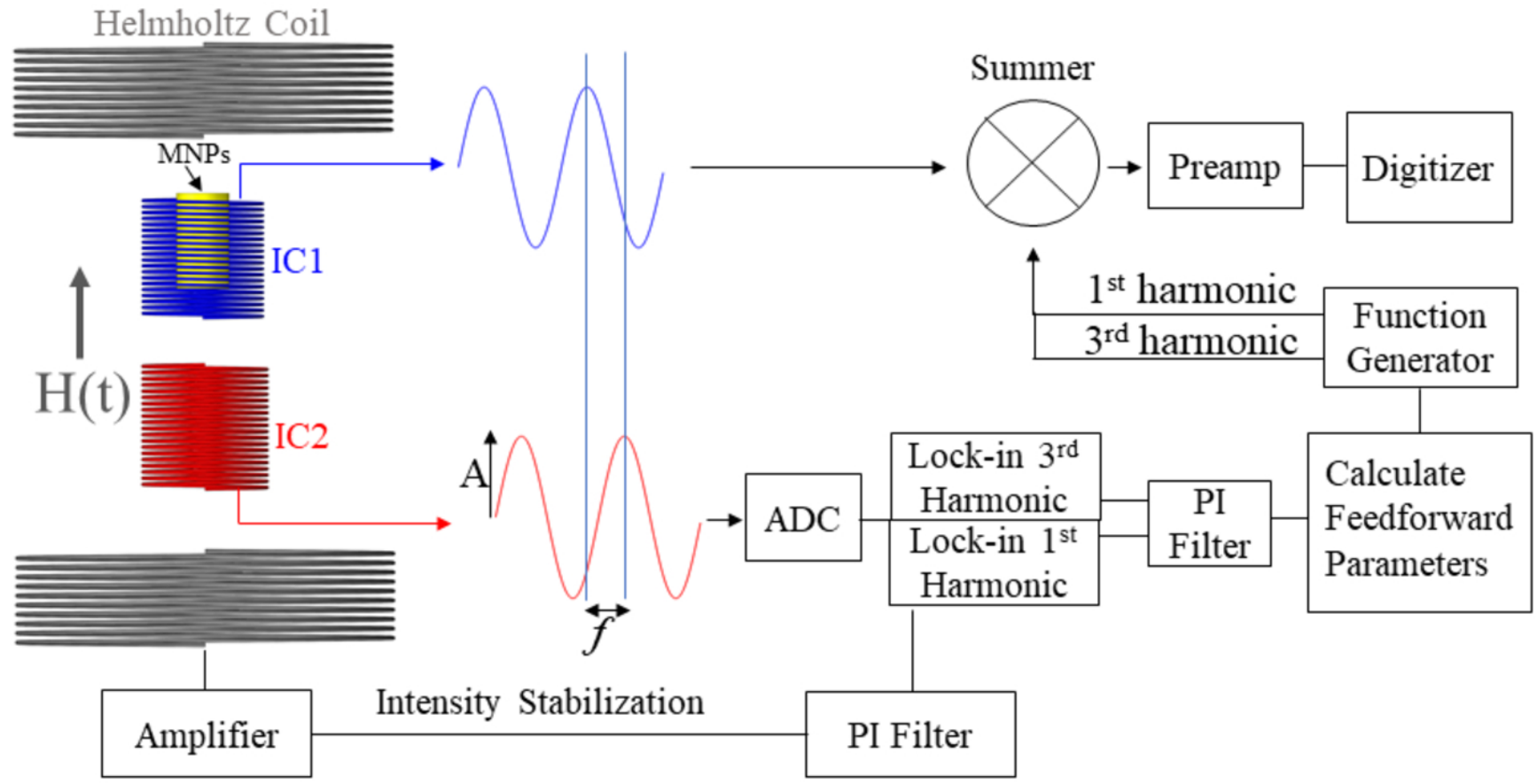
1. K. Wu, D. Su, R. Saha, J. Liu, V. K. Chugh and J.-P. Wang, *ACS Applied Nano Materials* **3** (6), 4972-4989 (2020).
2. N. Garraud, R. Dhavalikar, L. Maldonado-Camargo, D. P. Arnold and C. Rinaldi, *AIP Advances* **7**, 1-6 (2017).
3. Z. W. Tay, D. Hensley, J. Ma, P. Chandrasekharan, B. Zheng, P. Goodwill and S. Conolly, *IEEE Transactions on Medical Imaging* **38**, 2389-2399 (2019).
4. Q. A. Pankhurst, J. Connolly, S. K. Jones and J. Dobson, *Journal of Physics D: Applied Physics* **36** (13), R167-R181 (2003).
5. Y. Sun, M. B. Salamon, K. Garnier and R. S. Averback, *Physical Review Letters* **91** (16), 167206 (2003).
6. E. Hee Kim, H. Sook Lee, B. Kook Kwak and B.-K. Kim, *Journal of Magnetism and Magnetic Materials* **289**, 328-330 (2005).
7. S. Biederer, T. Knopp, T. F. Sattel, K. Lüdtke-Buzug, B. Gleich, J. Weizenecker, J. Borgert and T. M. Buzug, *Journal of Physics D: Applied Physics* **42** (2009).
8. F. Ludwig, D. Eberbeck, N. Löwa, U. Steinhoff, T. Wawrzik, M. Schilling and L. Trahms, *Biomedizinische Technik. Biomedical engineering* **58** (6), 535-545 (2013).
9. N. Garraud, R. Dhavalikar, M. Unni, S. Savliwala, C. Rinaldi and D. P. Arnold, *Physics in medicine and biology* **63** (17), 175016 (2018).
10. Z. W. Tay, D. W. Hensley, P. Chandrasekharan, B. Zheng and S. M. Conolly, *IEEE Transactions on Medical Imaging* **PP**, 1-1 (2019).
11. M. M. v. d. Loosdrecht, S. Draack, S. Waanders, J. G. L. Schlieff, H. J. G. Krooshoop, T. Viereck, F. Ludwig and B. t. Haken, *Review of Scientific Instruments* **90** (2), 024101 (2019).
12. T. Viereck, S. Draack, M. Schilling and F. Ludwig, *Journal of Magnetism and Magnetic Materials* **475**, 647-651 (2019).
13. M. Graeser, A. Von Gladiss, M. Weber and T. M. Buzug, *Physics in medicine and biology* **62**, 3378-3391 (2017).
14. M. Graeser, T. Knopp, P. Szwargulski, T. Friedrich, A. Von Gladiss, M. Kaul, K. M. Krishnan, H. Ittrich, G. Adam and T. M. Buzug, *Scientific Reports* **7**, 1-13 (2017).
15. D. Pantke, N. Holle, A. Mogarkar, M. Straub and V. Schulz, *Medical Physics* **46**, 4077-4086 (2019).
16. K. Wu, D. Su, R. Saha, D. Wong and J. P. Wang, *Journal of Physics D: Applied Physics* **15** (2019).
17. J. H. Hankiewicz, Z. Celinski, K. F. Stupic, N. R. Anderson and R. E. Camley, *Nature Communications* **7**, 1-8 (2016).
18. J. Salamon, J. Dieckhoff, M. G. Kaul, C. Jung, G. Adam, M. Möddel, T. Knopp, S. Draack, F. Ludwig and H. Ittrich, *Scientific Reports* **10** (1), 7480 (2020).
19. B. R. J. Stehning C.; Gleich, *International Journal on Magnetic Particle Imaging* **2**, 1-6 (2016).
20. J. Wells, H. Paysen, O. Kosch, L. Trahms and F. Wiekhorst, *AIP Advances* **8** (2018).
21. J. Zhong, M. Schilling and F. Ludwig, *Measurement Science and Technology* **29** (2018).
22. J. B. Weaver, A. M. Rauwerdink and E. W. Hansen, *Medical Physics* **36**, 1822-1829 (2009).
23. J. Zhong, W. Liu, L. Kong and P. C. Morais, *Scientific Reports* **4**, 1-5 (2014).
24. M. Zhou, J. Zhong, W. Liu, Z. Du, Z. Huang, M. Yang and P. C. Morais, *IEEE Transactions on Magnetics* **51** (2015).
25. S. Draack, T. Viereck, C. Kuhlmann, M. Schilling and F. Ludwig, *International Journal on Magnetic Particle Imaging; Vol 3, No 1 (2017)* **3**, 3-6 (2017).
26. S. Draack, T. Viereck, F. Nording, K. J. Janssen, M. Schilling and F. Ludwig, *Journal of Magnetism and Magnetic Materials* **474**, 570-573 (2019).

This is the author's peer reviewed, accepted manuscript. However, the online version of record will be different from this version once it has been copyedited and typeset.
PLEASE CITE THIS ARTICLE AS DOI: 10.1063/1.50031451

27. S. A. Shah, D. Reeves, R. M. Ferguson, J. B. Weaver and K. M. Krishnan, *Physical Review B - Condensed Matter and Materials Physics* **92**, 1-25 (2015).
28. Y. Shi and J. B. Weaver, *Medical Physics* **46**, 4070-4076 (2019).
29. S. Ota and Y. Takemura, *Journal of Physical Chemistry C* **123**, 28859-28866 (2019).
30. N. Garraud, R. Dhavalikar, M. Unni, S. Savliwala, C. Rinaldi and D. P. Arnold, *Physics in medicine and biology* **63** (2018).
31. Z. W. Tay, P. W. Goodwill, D. W. Hensley, L. A. Taylor, B. Zheng and S. M. Conolly, *Scientific Reports* **6**, 1-12 (2016).
32. P. W. Goodwill, E. U. Saritas, L. R. Croft, T. N. Kim, K. M. Krishnan, D. V. Schaffer and S. M. Conolly, *Advanced Materials* **24**, 3870-3877 (2012).
33. M. Graeser, T. Knopp, M. Grüttner, T. F. Sattel and T. M. Buzug, *Medical Physics* **40** (4), 042303 (2013).
34. B. Zheng, P. W. Goodwill, N. Dixit, D. Xiao, W. Zhang, B. Gunel, K. Lu, G. C. Scott and S. M. Conolly, *IEEE Transactions on Biomedical Circuits and Systems* **11**, 1041-1052 (2017).
35. J. Dieckhoff, D. Eberbeck, M. Schilling and F. Ludwig, *Journal of Applied Physics* **119** (2016).
36. Reference is made to commercial products to adequately specify the experimental procedures involved. Such identification does not imply recommendation or endorsement by the National Institute of Standards and Technology, nor does it imply that these products are the best for the purpose specified.

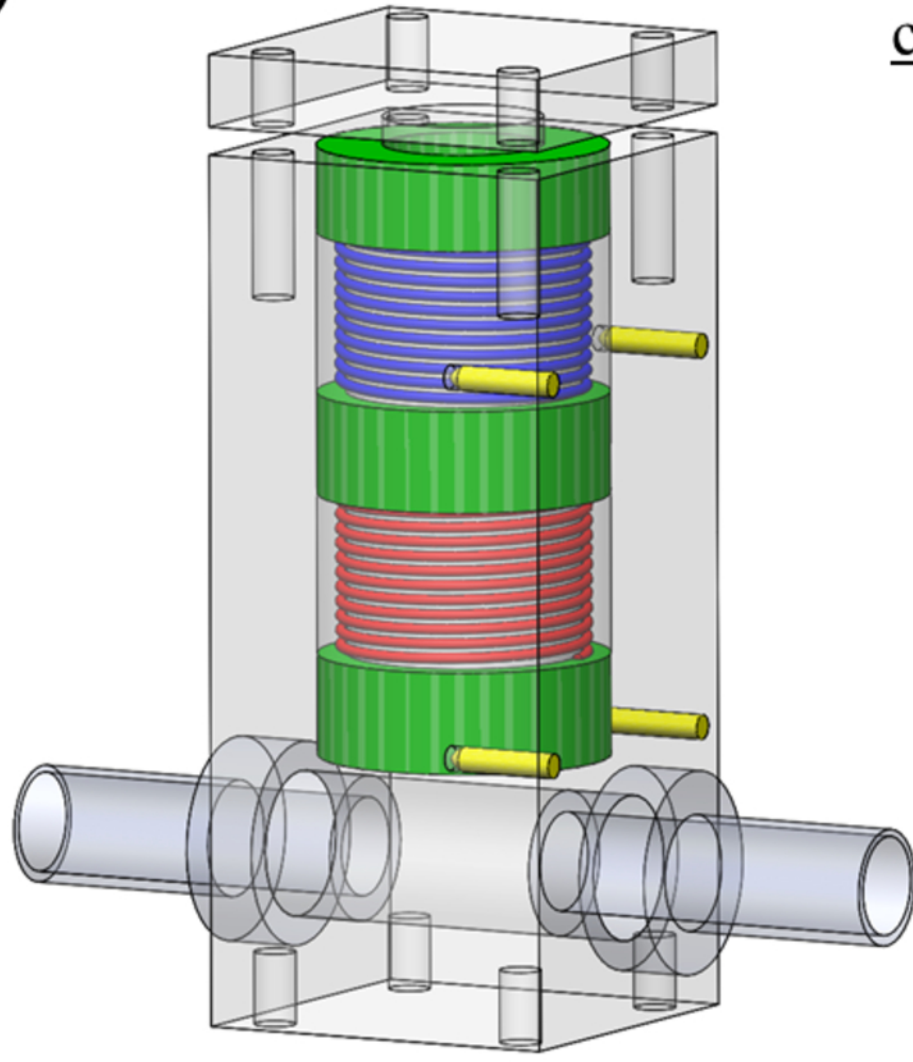
This is the author's peer reviewed, accepted manuscript. However, the online version of record will be different from this version once it has been copyedited and typeset.
PLEASE CITE THIS ARTICLE AS DOI: 10.1063/5.0031451

(a)

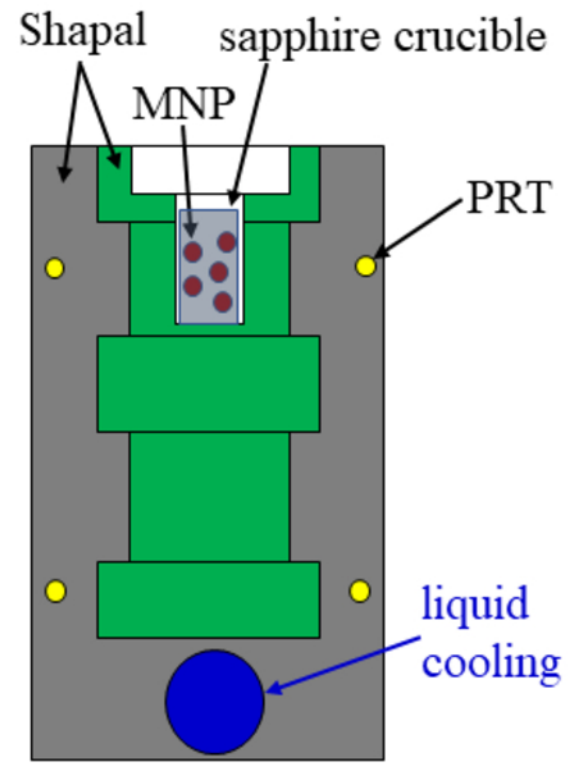


This is the author's peer reviewed, accepted manuscript. However, the online version of record will be different from this version once it has been copyedited and typeset.
PLEASE CITE THIS ARTICLE AS DOI: 10.1063/5.0031451

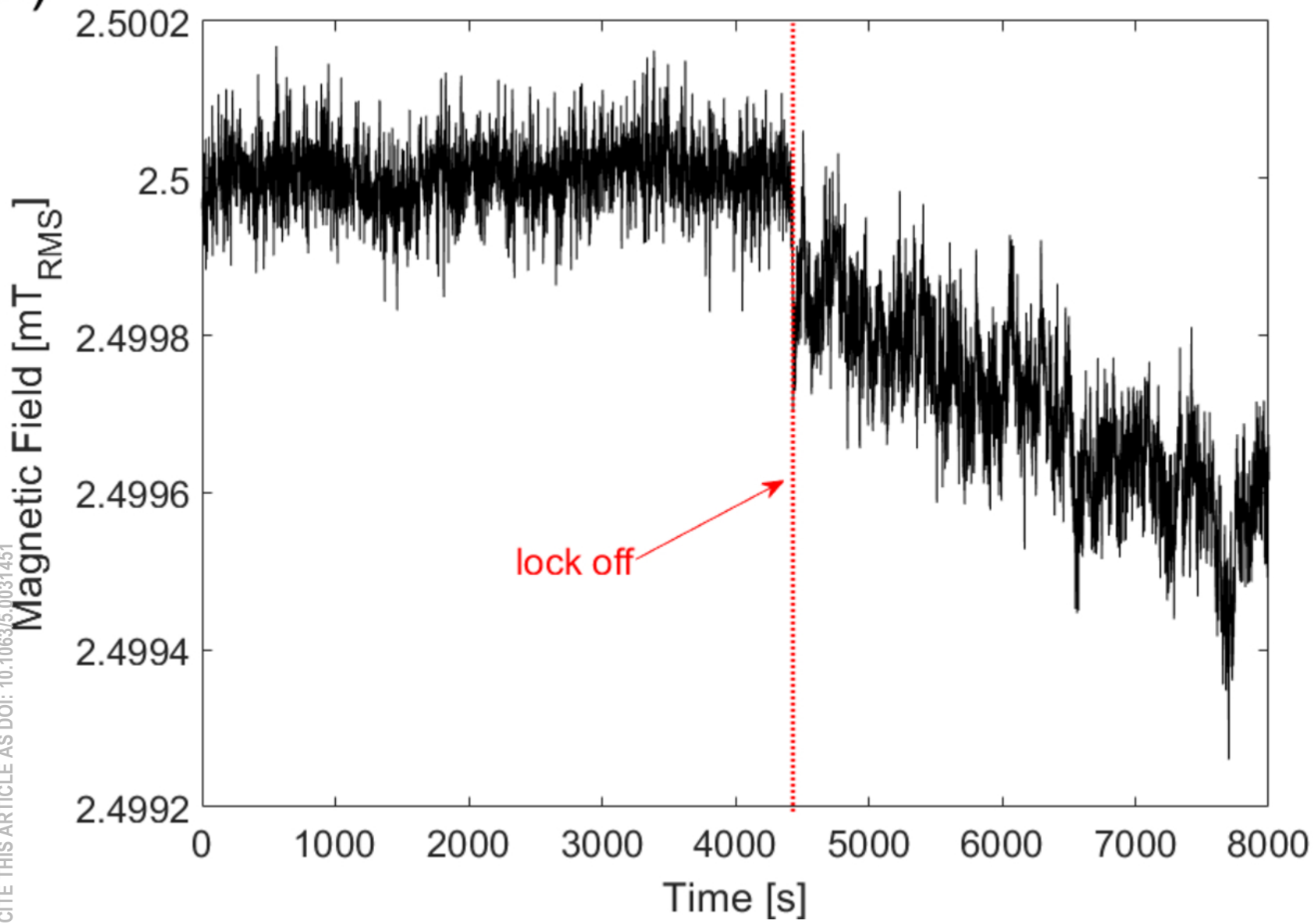
(b)



cross-sectional view

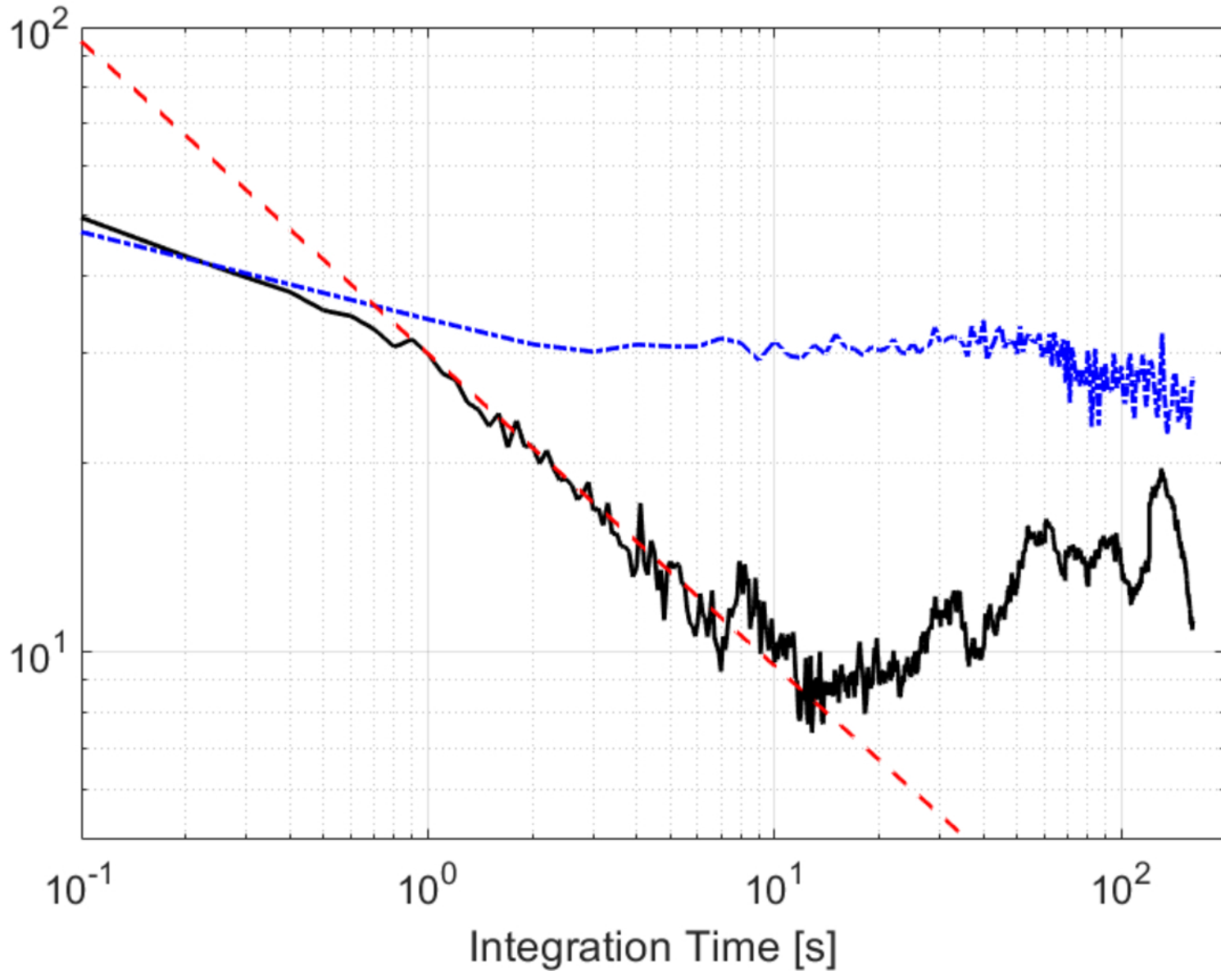


This is the author's peer reviewed, accepted manuscript. However, the online version of record will be different from this version once it has been copyedited and typeset.
PLEASE CITE THIS ARTICLE AS DOI: 10.1063/5.0031451

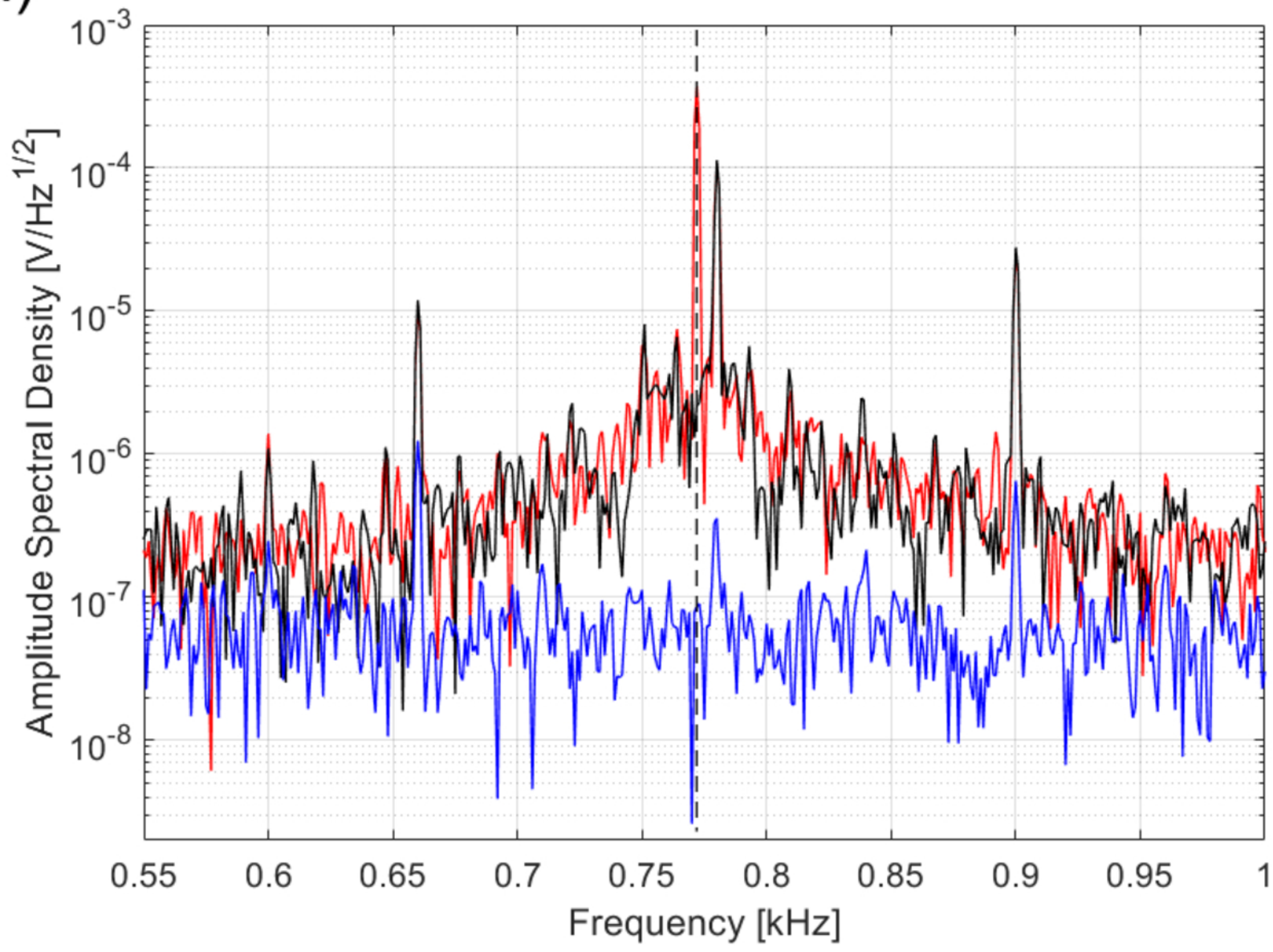
(a)

This is the author's peer reviewed, accepted manuscript. However, the online version of record will be different from this version once it has been copyedited and typeset.
PLEASE CITE THIS ARTICLE AS DOI: 10.1063/5.0031451

(b)
Allan Deviation [nT_{RMS}]

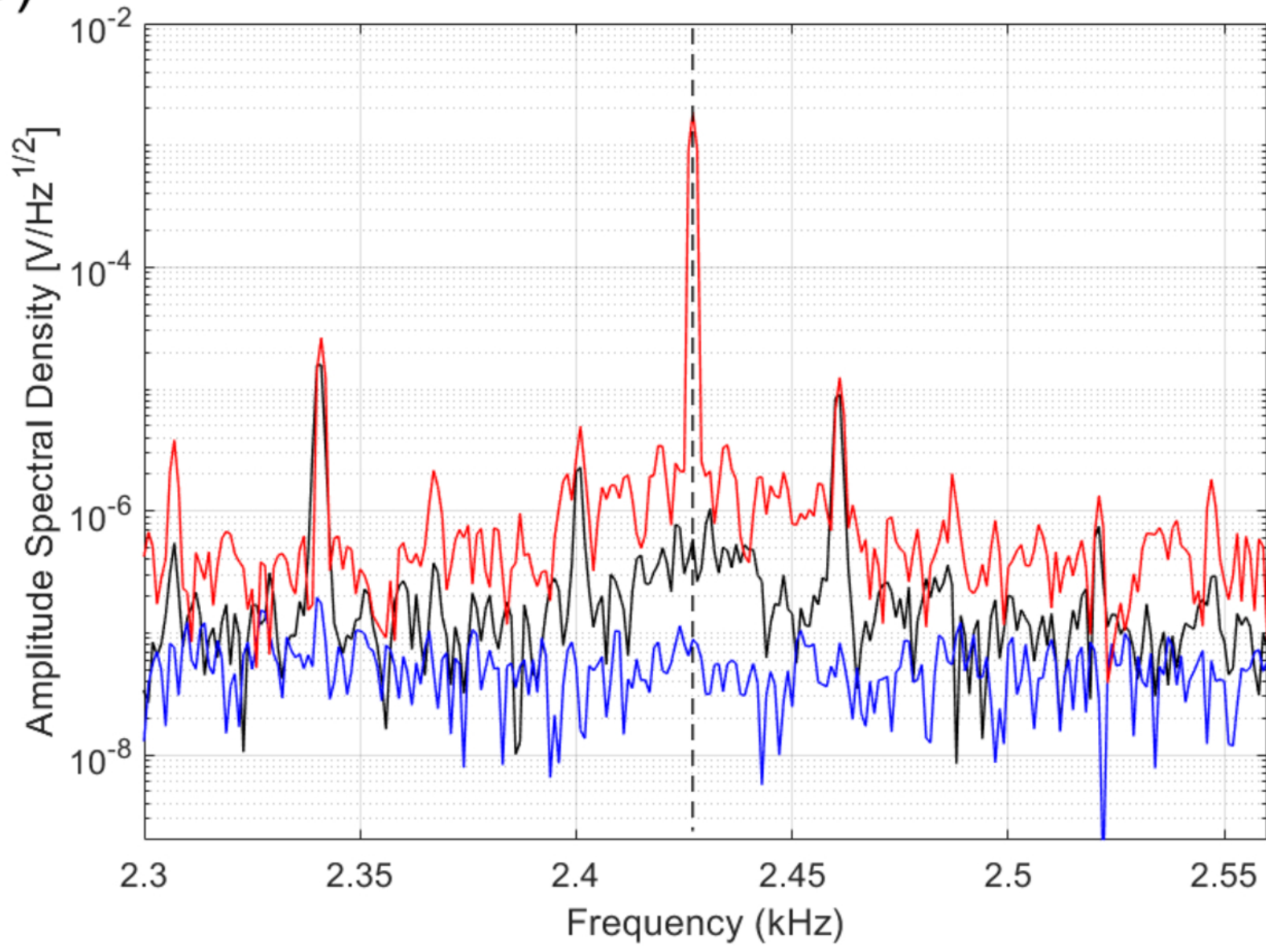


This is the author's peer reviewed, accepted manuscript. However, the online version of record will be different from this version once it has been copyedited and typeset.
PLEASE CITE THIS ARTICLE AS DOI: 10.1063/5.0031451

(a)

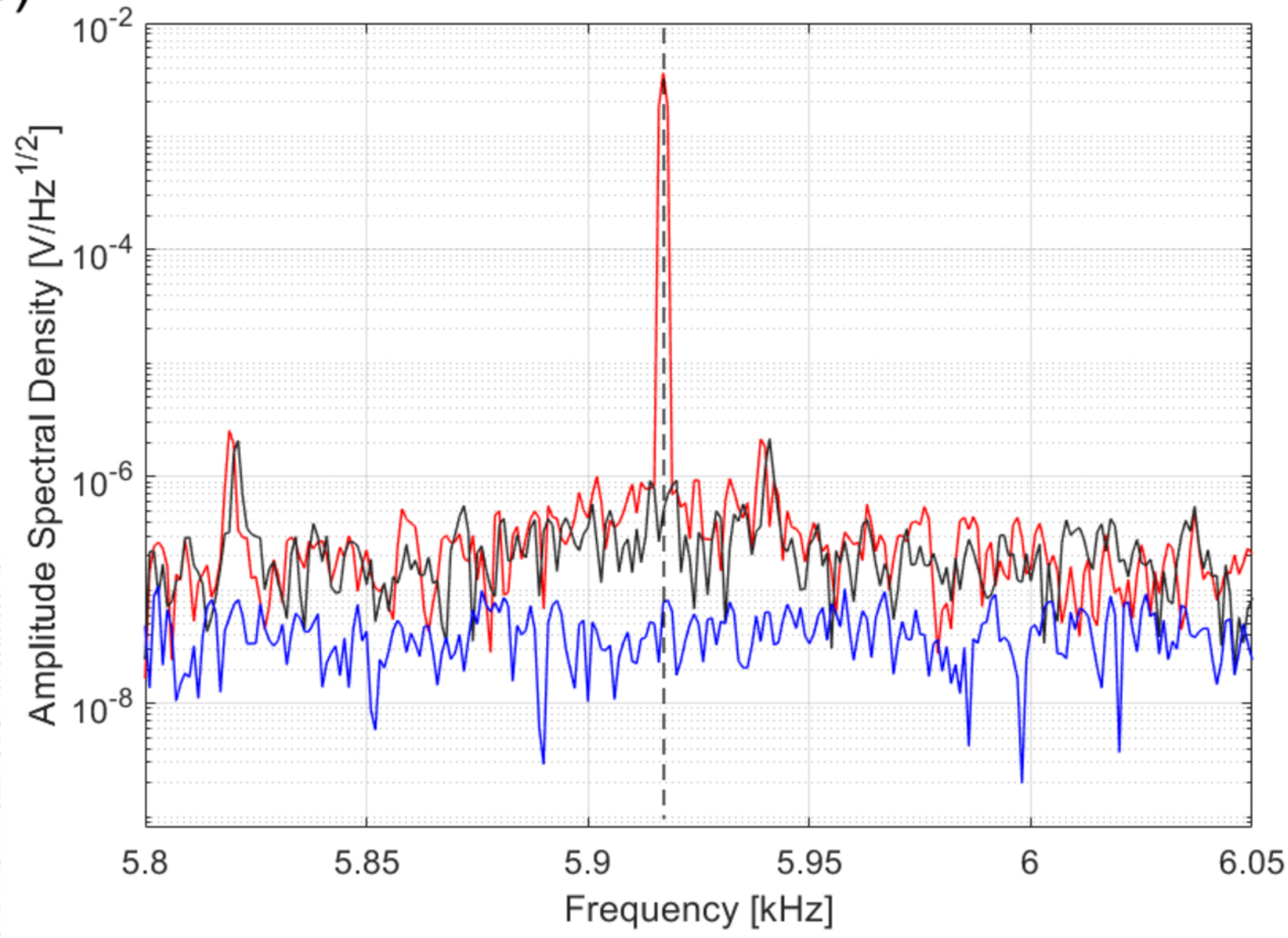
This is the author's peer reviewed, accepted manuscript. However, the online version of record will be different from this version once it has been copyedited and typeset.
PLEASE CITE THIS ARTICLE AS DOI: 10.1063/5.0031451

(b)

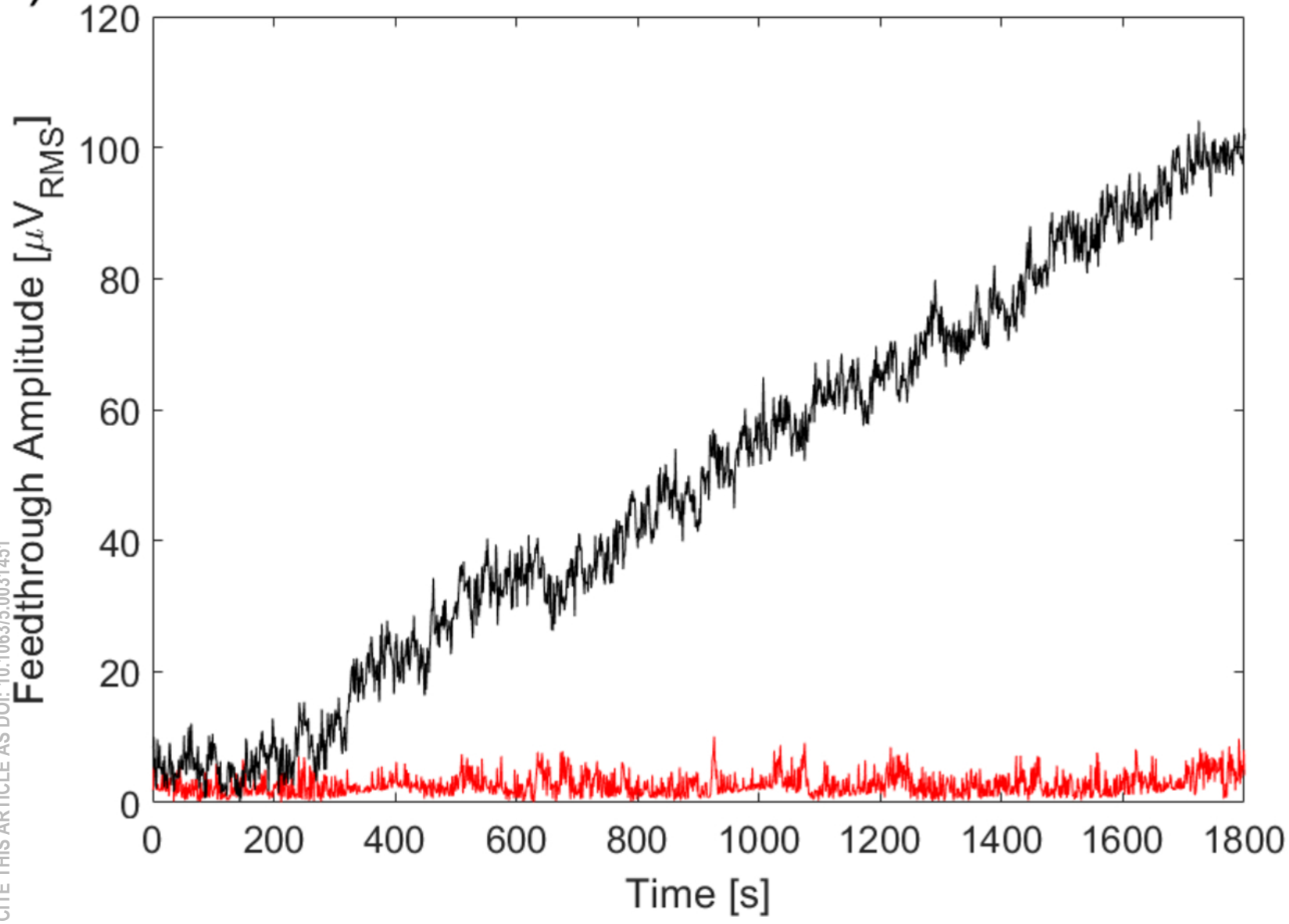


This is the author's peer reviewed, accepted manuscript. However, the online version of record will be different from this version once it has been copyedited and typeset.
PLEASE CITE THIS ARTICLE AS DOI: 10.1063/5.0031451

(c)

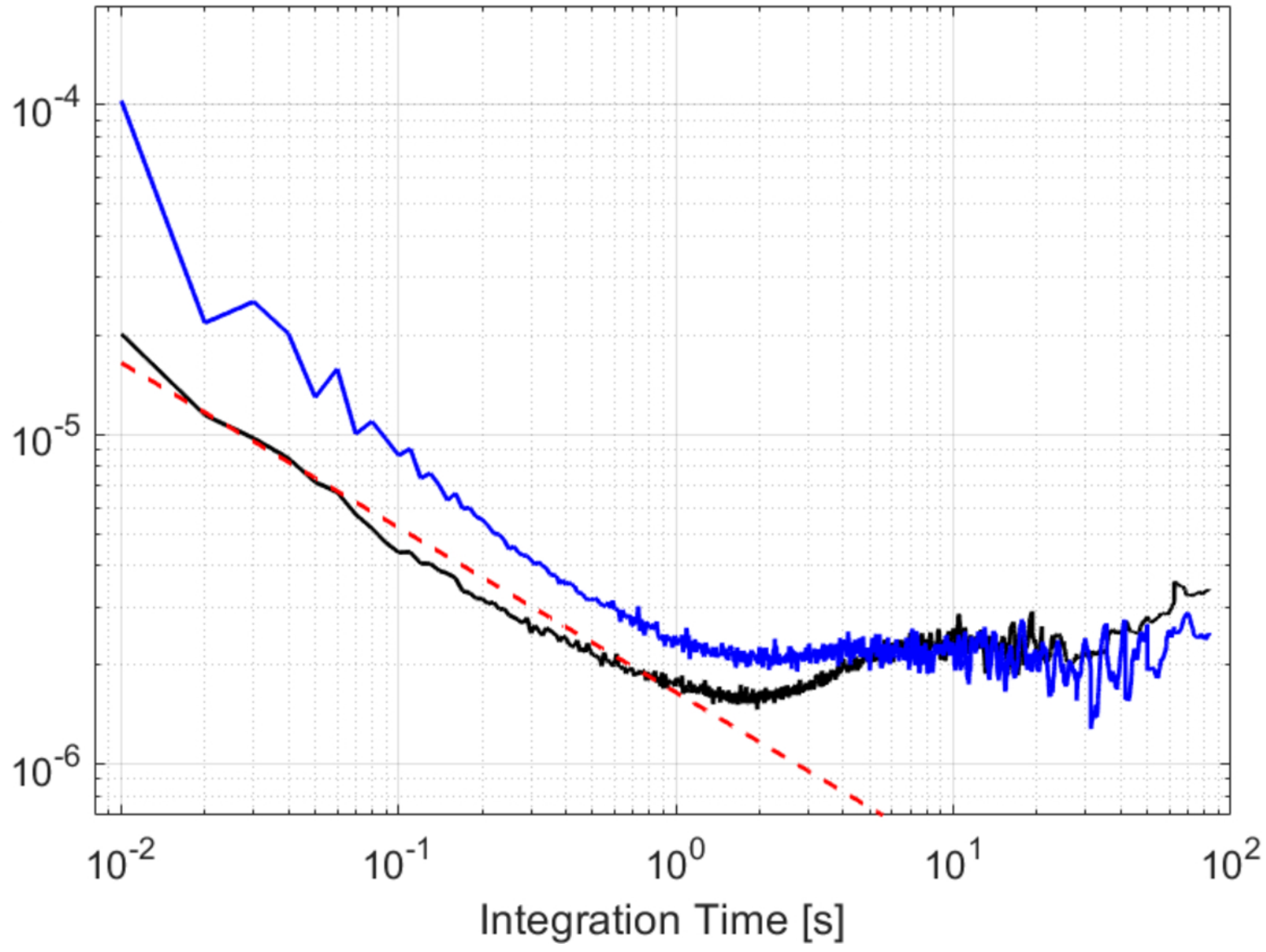


This is the author's peer reviewed, accepted manuscript. However, the online version of record will be different from this version once it has been copyedited and typeset.
PLEASE CITE THIS ARTICLE AS DOI: 10.1063/5.0031451

(a)

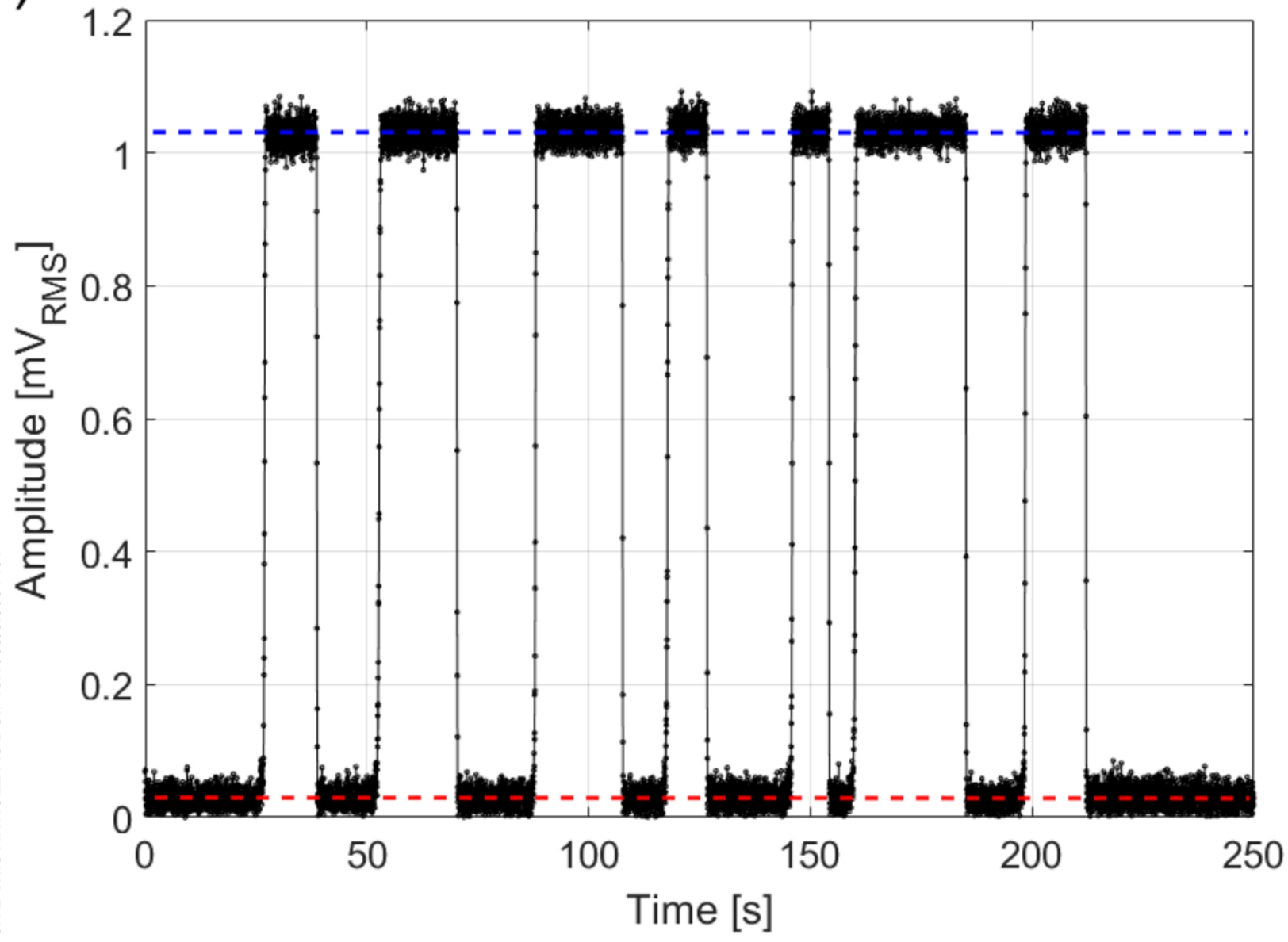
This is the author's peer reviewed, accepted manuscript. However, the online version of record will be different from this version once it has been copyedited and typeset.
PLEASE CITE THIS ARTICLE AS DOI: 10.1063/5.0031451

(b)
Allan Deviation [V_{RMS}]



This is the author's peer reviewed, accepted manuscript. However, the online version of record will be different from this version once it has been copyedited and typeset.
PLEASE CITE THIS ARTICLE AS DOI: 10.1063/5.0031451

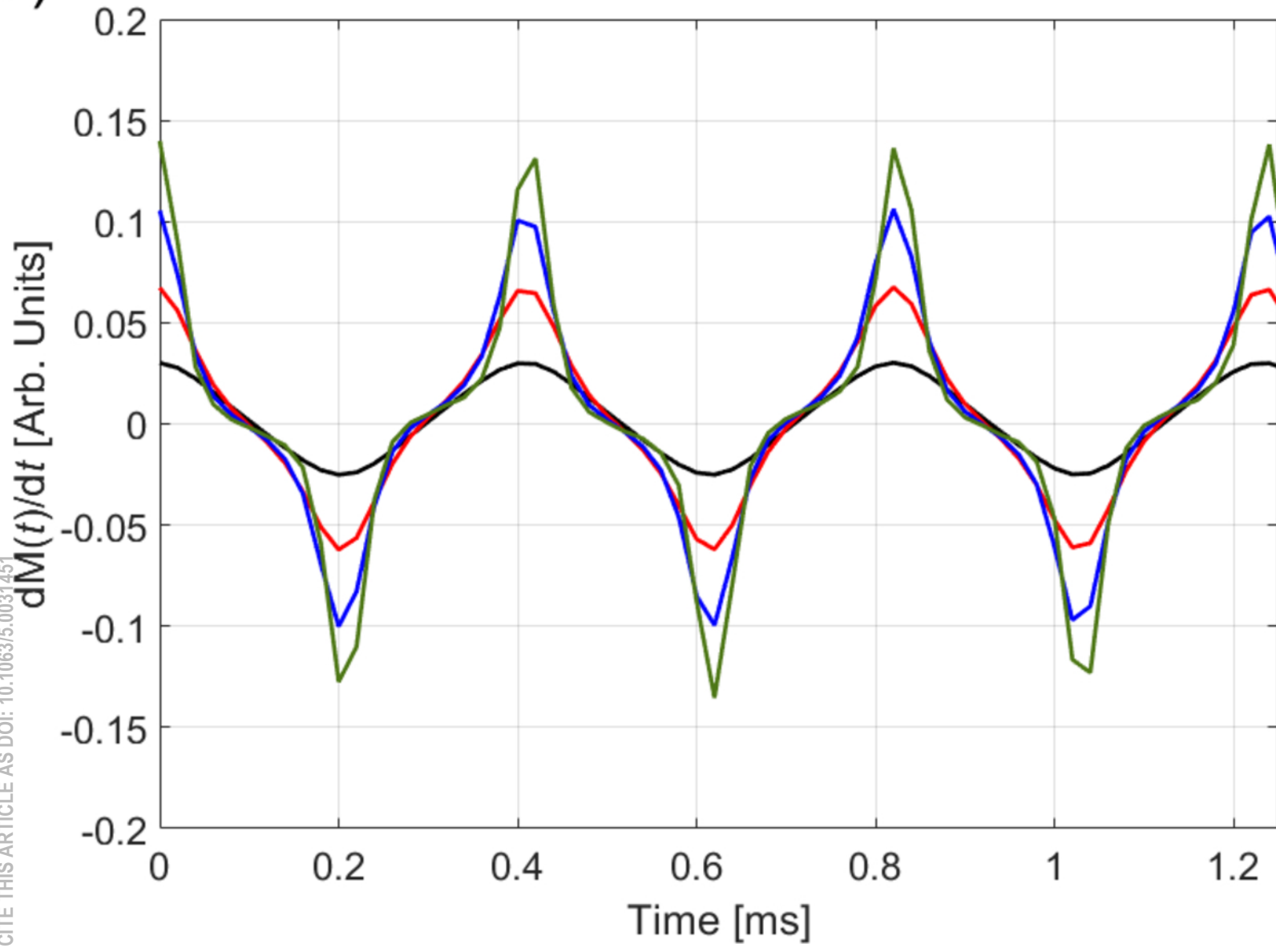
(c)



This is the author's peer reviewed, accepted manuscript. However, the online version of record will be different from this version once it has been copyedited and typeset.

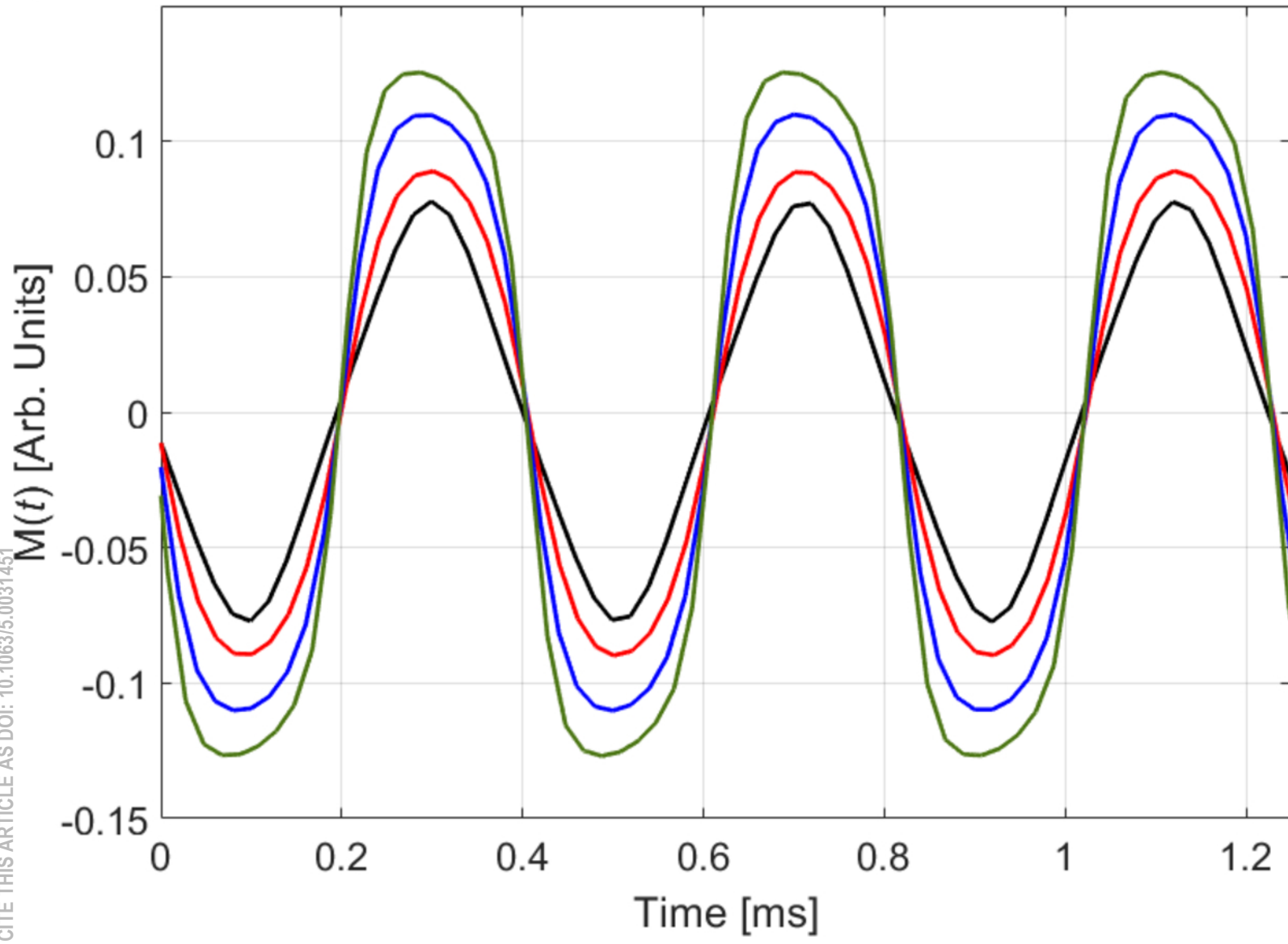
PLEASE CITE THIS ARTICLE AS DOI: 10.1063/5.0031451

(a)



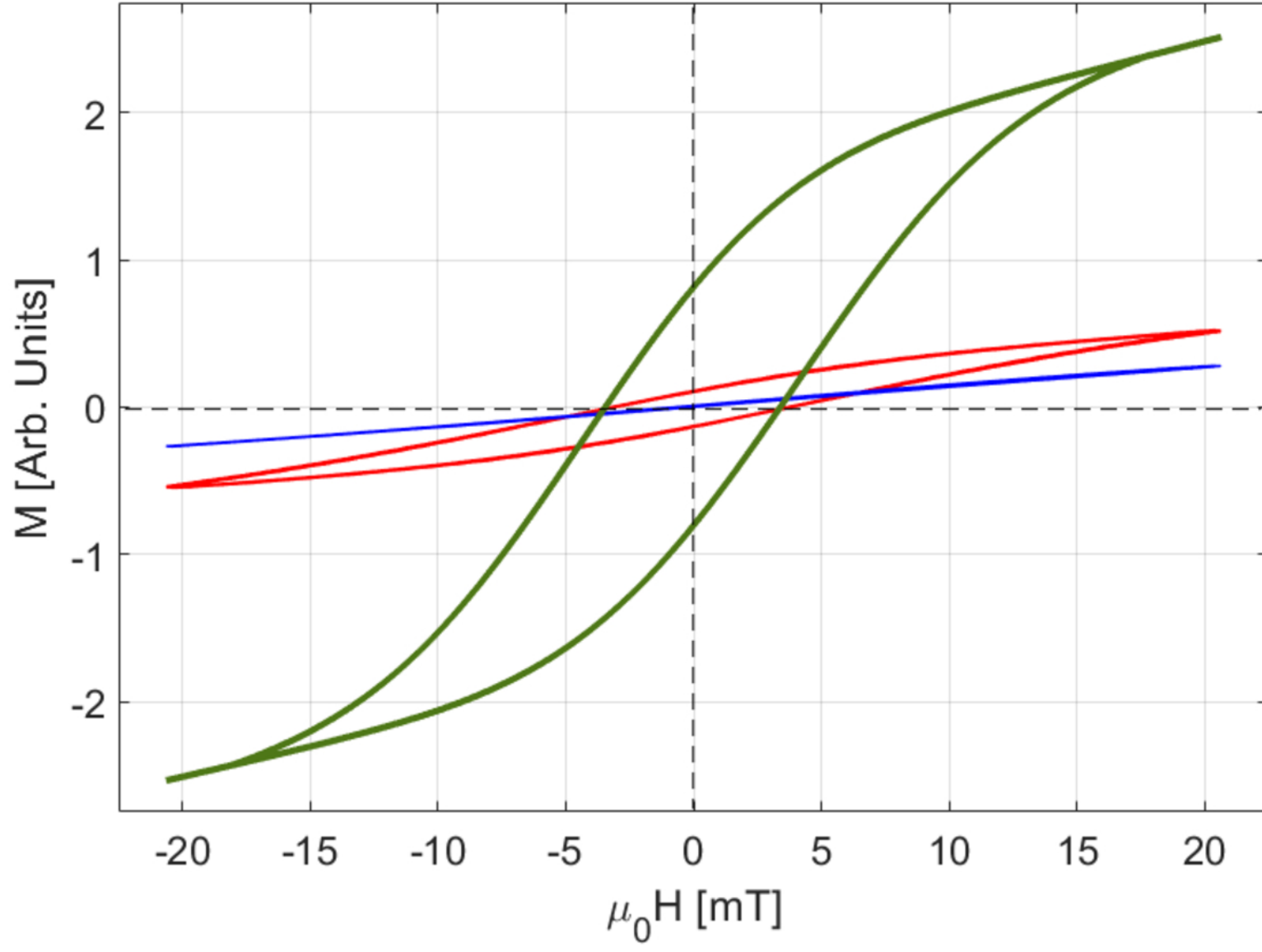
This is the author's peer reviewed, accepted manuscript. However, the online version of record will be different from this version once it has been copyedited and typeset.
PLEASE CITE THIS ARTICLE AS DOI: 10.1063/5.0031451

(b)

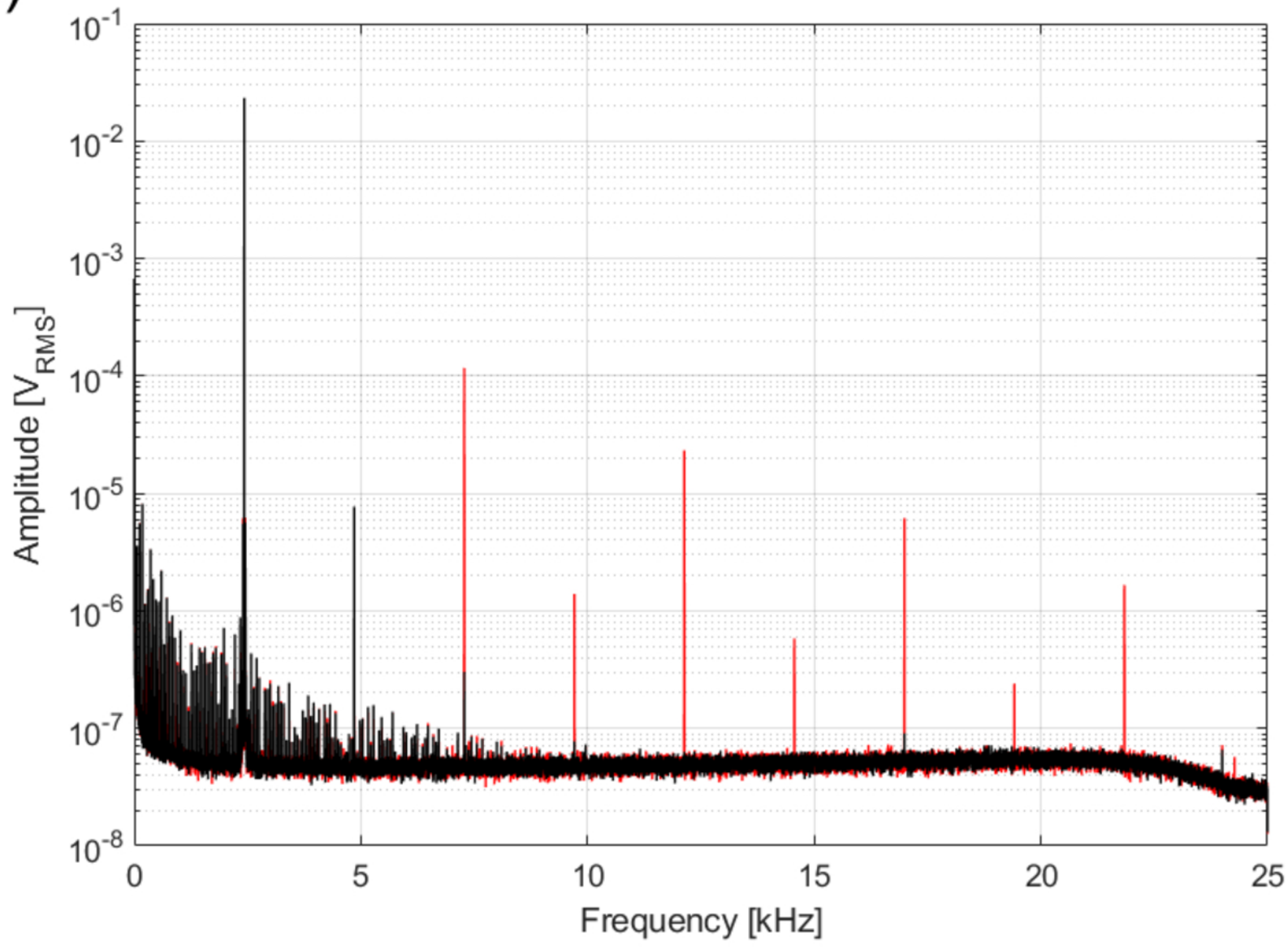


This is the author's peer reviewed, accepted manuscript. However, the online version of record will be different from this version once it has been copyedited and typeset.
PLEASE CITE THIS ARTICLE AS DOI: 10.1063/5.0031451

(c)

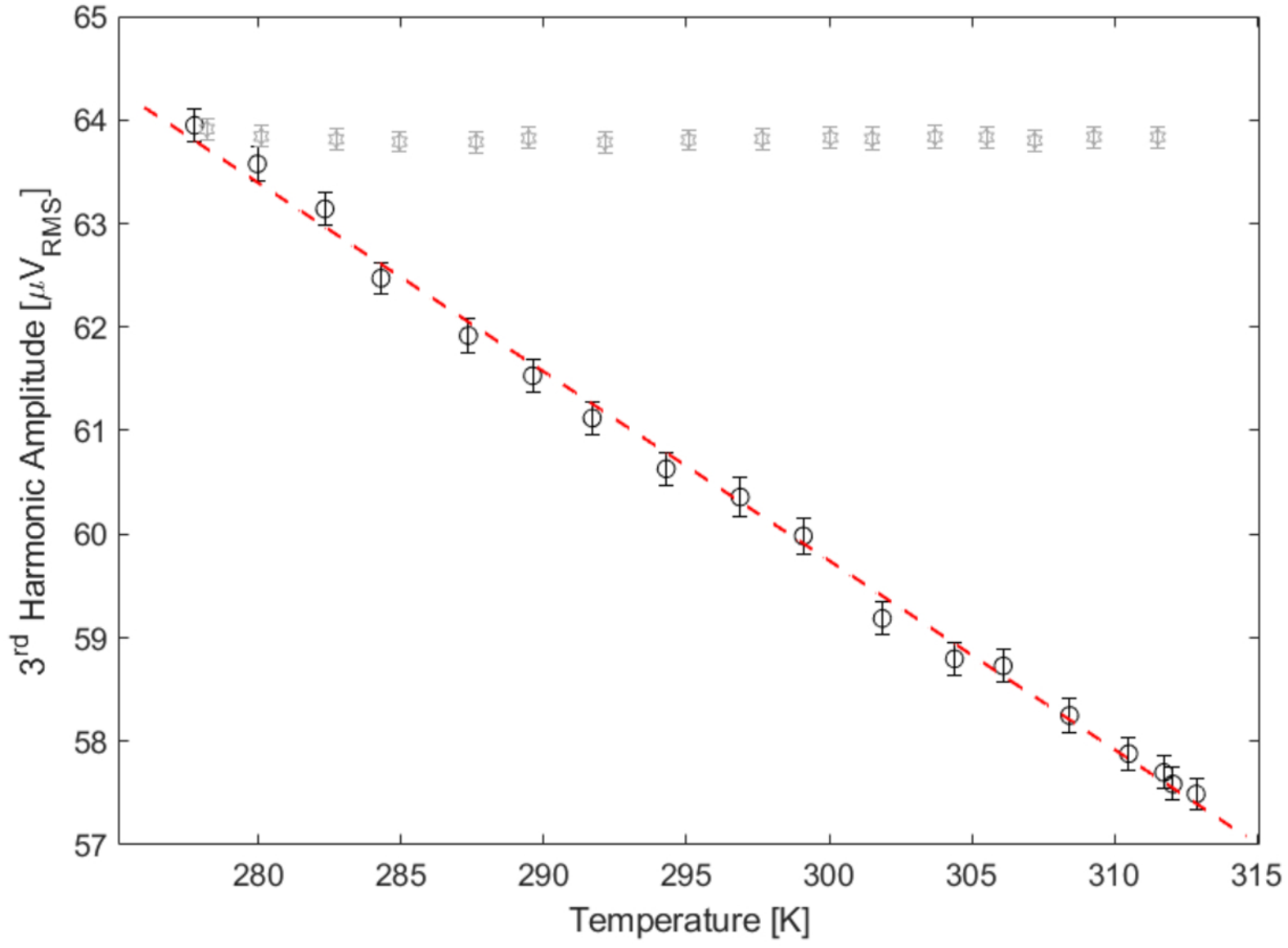


This is the author's peer reviewed, accepted manuscript. However, the online version of record will be different from this version once it has been copyedited and typeset.
PLEASE CITE THIS ARTICLE AS DOI: 10.1063/5.0031451

(a)

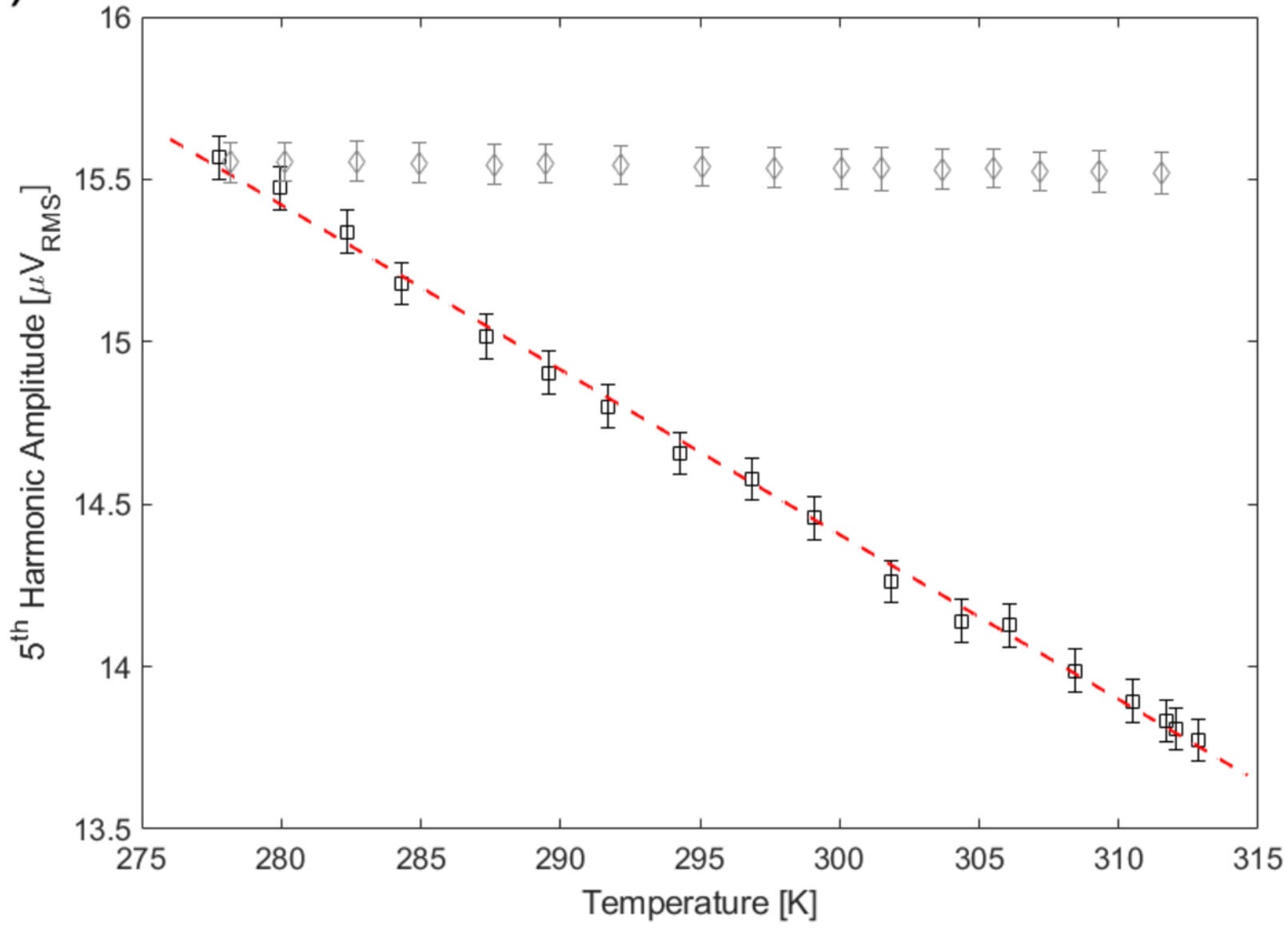
This is the author's peer reviewed, accepted manuscript. However, the online version of record will be different from this version once it has been copyedited and typeset.
PLEASE CITE THIS ARTICLE AS DOI: 10.1063/5.0031451

(b)



This is the author's peer reviewed, accepted manuscript. However, the online version of record will be different from this version once it has been copyedited and typeset.
PLEASE CITE THIS ARTICLE AS DOI: 10.1063/5.0031451

(c)



This is the author's peer reviewed, accepted manuscript. However, the online version of record will be different from this version once it has been copyedited and typeset.

PLEASE CITE THIS ARTICLE AS DOI: 10.1063/5.0031451

(d)

